REVIEW

ADVANCED MATERIALS TECHNOLOGIES
www.advmattechnol.de

Progress and Prospects of Nanoscale Emitter Technology for AR/VR Displays

*Sun Jae Park, Changmin Keum, Huanyu Zhou, Tae-Woo Lee, Wonhee Choe, and Himchan Cho**

Augmented reality (AR) and virtual reality (VR) are emerging interactive technologies that realize the "metaverse," leading to a totally new digital interactive experience in daily life in various aspects. In order to provide users with a more immersive experience, displays for AR/VR have rapidly evolved to achieve high resolutions and a large color gamut on small panels. Recently, nanoscale light emitters such as quantum dots (QDs) and metal halide perovskites (MHPs) with high photoluminescence quantum efficiency and color purity levels have garnered much attention as color conversion materials in AR/VR displays. However, the low material stability and the absence of a high-resolution patterning process that does not impair the optical properties of nanoscale emitters act as obstacles preventing the realization of high-resolution AR/VR displays. Here, the state-of-the-art technologies constituting current AR/VR devices are reviewed from an industrial point of view and the recent progress in QD and MHP emitter technologies are discussed, including their basic structural properties, synthesis strategies to enhance the stability, advanced patterning technologies, down-conversion and light-emitting diode applications. Based on the review, the authors' perspective on future research directions of nanoscale emitters for next-generation AR/VR displays is presented.

1. Introduction

As metaverse will enter our daily lives in the near future in various aspects, the realization of augmented reality (AR) and virtual reality (VR) technologies is an emerging issue, which is attracting considerable amounts of attention. Because both AR and VR technologies require the successful implementation of a virtual world and/or digital information, the performance of the AR/VR devices providing the information is significant. The wearable device form factor is preferred for AR/VR displays, with examples being head-mounted displays (HMDs) or near-eye-displays (NEDs) (e.g., smart glasses). Although significant improvements have been made over the past ten years with regard to AR/VR technologies,[1–5] challenges such as light loss in the optical system and limited resolutions of displays inhibit the realization of an metaverse-based future. In order to realize a high-definition display with a realistic and immersive experience on a thin/light device, efforts to break through the limits of existing technology in terms of materials and processes should be made.

The light-emitting materials play a key role in the development of a high-performance display, and recently, emerging nanoscale emitters are attracting much attention in this area. Particularly, colloidal quantum dots (QDs) and metal halide perovskites (MHPs) are in the spotlight for realizing natural colors and realistic images in such next-generation displays, due to their high color purity (i.e., narrow emission spectra), high photoluminescence quantum

---

S. J. Park, H. Cho
Department of Materials Science and Engineering
Korea Advanced Institute of Science and Technology (KAIST)
291 Daehak-ro, Yuseong-gu, Daejeon 34141, Republic of Korea
E-mail: himchan@kaist.ac.kr

C. Keum
Samsung Research
Samsung Electronics Co. Ltd.
Seongchon-gil 34, Seocho-gu, Seoul 06765, Republic of Korea

H. Zhou, T.-W. Lee
Department of Materials Science and Engineering
Seoul National University
1 Gwanak-ro, Gwanak-gu, Seoul 08826, Republic of Korea

T.-W. Lee
School of Chemical and Biological Engineering
Institute of Engineering Research
Research Institute of Advanced Materials
Soft Foundry
Seoul National University
1 Gwanak-ro, Gwanak-gu, Seoul 08826, Republic of Korea

W. Choe
Department of Artificial Intelligence and Software
Ewha Womans University
52 Ewhayeodae-gil, Seodaemun-gu, Seoul 03760, Republic of Korea

The ORCID identification number(s) for the author(s) of this article can be found under https://doi.org/10.1002/admt.202201070.

DOI: 10.1002/admt.202201070

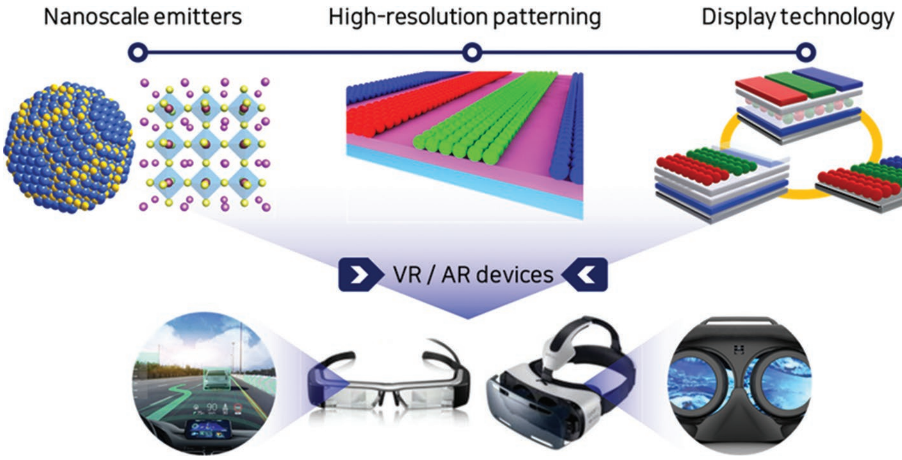

Figure 1. Overview of the requirements of the material/device aspects of AR/VR displays (Bottom images: adapted with permission.[245–247] AR and VR devices: image courtesy of Epson and Samsung, respectively.)

yield (PLQY), strong optical absorption, and color tunability.[6–11] Because of the unique optical properties, QDs and MHPs have become promising candidates for next-generation color-conversion layers[12–14] or electroluminescence (EL) emission layers[15–17] in display panels. The emission spectrum of QDs is tunable depending on the size of QDs due to the quantum size effect, which enables nearly 100% coverage of color volume and thus vibrant color of QD-based displays. In fact, the QDs have already been adopted to commercial products such as high-definition large-size TVs by Samsung and Others. In the products, QDs are incorporated in a color enhancement layer embedded between color filters and the backlight. The QD enhancement films composed of red/green QDs, resin and barrier films greatly increase the color gamut of displays by down-conversion PL; the QD enhancement film should be distinguished from the next-generation QD color filters implemented through QD pixel patterning, which will be discussed in the Section 5. The MHPs have narrower emission spectra than QDs, and thereby can realize a larger color gamut of ≈95% of Rec.2020 (cf., ≈85% of Rec.2020 for InP-based QDs).[18] Also, high absorption coefficient (higher than InP QDs), simple synthesis process, easy color tuning with substitution of halide moiety, and low material cost of MHPs make them a promising alternative to QDs.[19–21] However, industrial applications of MHP emitters (as a color conversion layer) have not been achieved so far mainly due to their fundamentally low material stability, which is discussed in Section 3.2.

The implementation of an immersive AR/VR display, especially for compact-size NEDs, requires a precise, high-resolution patterning of red, green, and blue (RGB) pixels; actually, the patterning process of RGB pixels includes patterning of a light source (e.g., blue micro light-emitting diodes (LEDs)), color conversion materials (e.g., QDs), and thin-film transistor (TFT) backplane. The required pixel resolution in the display panels of AR/VR devices is several thousand pixels per inch (PPI), where a pixel size is in the range of µm units. Particularly, ≈10 000 PPI is required for AR applications. However, many technical problems such as pattern nonuniformity and degradation of QDs limit the high-resolution patterning process. In this review, we briefly discuss the difficulties in patterning light sources and backplanes (Section 2) and mainly focus on the recent advances in various patterning methods of color conversion materials (Section 4).

The next-generation display type that might succeed the QD color filter is QD/MHP EL. QD EL displays have received great research interest for the past ten years because of their advantages including large color volume, high efficiency, wide viewing angle, high contrast, and thin panels.[6,7,22] Thus far, red and green self-emissive QD/MHP LEDs have achieved significant improvements, reaching external quantum efficiency (EQE) >20%,[23–25] but both emitters still have limitations with regard to the implementation of blue LEDs. Particularly, low operational lifetime of MHP LEDs (PeLEDs), typically shorter than those of QD LEDs (QLEDs), demands further intensive research in order for PeLED to catch up with QLEDs and OLEDs. Although it seems obvious that QD color filter displays will be on the market first, we believe that QD EL displays will provide a valuable display platform for future AR/VR NEDs. Recent advances and limitations of down-conversion PL and EL of QD/MHP emitters are discussed in Section 5.

Herein, we review the recent research progress of emerging nanoscale emitters as an essential requirement for realizing immersive AR/VR displays, mainly focusing on their use as a color conversion layer (**Figure 1**). In Section 2, we will review the recent trends of AR/VR device technologies in the industry and the key features to evaluate the performance capabilities of AR/VR devices. The recent research progress in QD and MHP emitter technologies is reviewed in Sections 3, 4, and 5, including their structural and optical properties, synthesis strategies, patterning methods, down-conversion PL, and EL applications. Finally, summary and our perspectives on future research directions of the QD and MHP emitters for AR/VR applications are provided in the Section 6.

2. Progress of Near-Eye Displays for AR/VR

2.1. Recent Progress in AR/VR Technology in the Industry

Since AR and VR appeared on the Gartner Hype Cycles for Emerging Technologies in 2006 and 2014, respectively,[26] AR/VR technologies have been continuously regarded as the next computing platforms with the potential to transform many aspects of our modern digital lives as well as to create a rapidly growing market. In the industry, an increasing number of tech companies have been developing AR/VR technologies with a variety of different strategies over the last decade.

AR technology is often defined as a set of technologies that overlays digital visual images and contents on the real-world scene. This concept includes smartphone-based AR, which provides the user computer-generated content overlaid on a real-world environment tracked by a camera on the device screen. Although numerous mobile AR apps have led to the creation of a massive market in the past few years, aimed at e-commerce, gaming, entertainment, and education, the user experience remains limited as users are required to hold a device in front of them and the physical screen diminishes reality. Such constraints have facilitated the advancement of AR devices in a wearable form factor.

Smart glasses are an eyewear device capable of providing digital information, typically 2D text and images, while allowing the user to view the real world through semi-transparent optical combiners. In light of the denotation of a true AR experience, that is, the user perceives the digital graphics as if they are seamless parts of the real world, smart glasses which simply displays information is essentially distinguished from high-end AR headsets. Instead, typical smart glasses provide real-time information and data via a display accessible in the user's field of view (FOV) with a hands-free feature, greatly improving workforce efficiency and worker safety. Along with Google, which launched the first publicly available product in 2014, technology companies such as Snap, Meta, and Vuzix are major developers in the smart glass market.

High-end AR systems require more complex hardware compositions for the display engine, combiner optics, and optical sensors than smart glasses. Particularly, advanced sensor systems are a core additional building block to gather sufficient 3D information about the surrounding environment while tracking the relative position of the user to enable AR, including depth scanning sensors, head-trackers supporting six-degree-of-freedom (DOF) movement, eye trackers, and gesture sensors. Although the aim is to shrink the form factor eventually such that the devices can be considered as AR "glasses," the current direction of development uses the form of a headset (e.g., Microsoft Hololens 2 and Magic Leap One) due to the most demanding cutting-edge hardware. To date, the majority of smart glasses and AR headsets are oriented to use by enterprises, such as those related to construction, warehouse logistics, and manufacturing, among others, while industry continues putting much effort into developing products that meet consumer expectations.

In contrast to AR devices, the primary aim of VR technology is to provide the user with fully immersive virtual experiences by only showing computer-generated content while completely blocking the real-world vision. Thus, VR devices are relevant to indoor activities with limited mobility, and currently main use cases are found in gaming, that is, as VR gaming systems. Early VR headsets were used while tethered to a computer capable of supporting high-quality rendering and synchronized with outside-in head-tracking sensors installed in a VR-dedicated space. Currently, the VR headset hardware architecture has evolved toward a standalone solution with inside-out sensors offering 6DOF VR experiences (e.g., Meta Oculus Quest 2 and HTC Vive Focus Plus). The key display and optics specifications of several commercial AR/VR devices are summarized in **Table 1**.

Table 1. Comparison of commercial AR/VR NEDs.[237]

Form factor	Name	Display type	Optics (imaging, combiner)	FOV	Resolution (per-eye)	Year
Smart glasses	Google Glass Enterprise Edition 2	lCoS (monocular)	Prism	13° hori	640 × 360	2019
	Vuzix M4000	DLP (monocular)	waveguide	28° diag	854 × 480	2020
	Oppo Air Glass	Monochrome microLED (monocular)	waveguide	28° diag	640 × 480	2022
	Realwear HMT-1	LCD (monocular)	N/A	20° hori	854 × 480	2017
AR headsets	Microsoft Hololens 2	LBS (binocular)	waveguide	52° diag	1440 × 936	2019
	Magic Leap One	lCoS (binocular)	waveguide	40° hori	1280 × 960	2018
VR headsets	Oculus Quest 2	LCD (binocular)	Fresnel lenses	97° hori	1832 × 1920	2020
	HTC Vive Pro 2	LCD (binocular)	Fresnel lenses	116° hori	2448 × 2448	2021
	Sony PlayStation VR	OLED (binocular)	Aspherical lenses	96° hori	960 × 1080	2016

Hori: horizontal, diag: diagonal.

While the device architectures of smart glasses and AR/VR headsets are designed differently depending on their core functionalities, mostly in terms of the optical systems used, several common challenges related to their similarity as NED or HMD types of form factors must be addressed. In NEDs, the light radiated from the display panel travels through intermediate optics located in close proximity to the eyes, that is, within a few centimeters. Thus, several optical factors, such as the eyebox, FOV, angular resolution, and brightness, must carefully be taken into account to satisfy human visual and comfort requirements. In addition, NED devices must facilitate wearable comfort while also being lightweight and with a balanced center of gravity, a suitable size, good thermal management, and a socially acceptable shape. This means that a complete paradigm shift is required from conventional flat-panel displays such as TVs, monitors, tablets, and smartphones when designing optical systems, and an in-depth understanding of the features of human visual perception and optical limitations becomes crucial.

2.2. Key Optical Features of AR/VR Headsets

The FOV of NEDs is the angular extent over which a virtual image is perceived by the viewer. Typically, the entire FOV of the human vision system spans 220° horizontally, and the overlapped range of binocular vision is as wide as 120°.[26] Thus, an FOV which is sufficiently large to cover the human vision system is required to provide a fully immersive experience. Most state-of-the-art VR headsets, such as the Oculus Quest 2, HTC Vive Pro, and Sony PlayStation VR types, have a horizontal FOV of around 100° to 110°, while a few companies such as Pimax and StarVR announced products with a horizontal FOV that exceeds 200°.[27] On the other hand, the FOV of AR headsets is limited to around 40° to 50° in the diagonal direction (e.g., Magic Leap One and Microsoft Hololens 2), and typical smart glasses have even smaller diagonal FOVs of around 15° to 35°.[28] The eyebox defines the spatial region in which entire FOV of a virtual image is viewed by the eye without vignetting. A larger eyebox can accommodate a greater range of the interpupillary distance (IPD) from different user populations and can offer more flexibility with regard to eye movement or the displacement of headsets. The angular resolution defines the number of pixels per degree (PPD) in the virtual image, i.e., the ratio of the pixel resolution of the display panel to the FOV (**Figure 2**). In case of AR/VR displays, an optical system is often incorporated in front of the display panel to expand FOV. However, according to the definition of PPD, the FOV and the PPD are essentially in trade-off relationship, while the PPI metric is fixed. Therefore, it is desirable to use the PPD metric instead of PPI for NEDs to properly reflect user's experience. A human eye with normal visual acuity (commonly referred to as 20/20 vision) is able to resolve a spatial pattern separated by one arcmin, which corresponds to 60 PPD.[29] To achieve both a high angular resolution and a large FOV, the most straightforward approach is to increase the number of pixels of the display panel. However, increasing the pixel resolution becomes challenging, particularly for micro-displays, due to physical limitations on the reduction of the pixel size, which will be discussed in detail later.

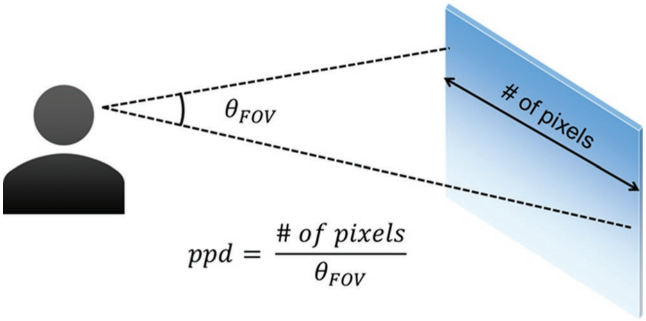

Figure 2. Schematic representation of the definition of PPD.

In an optical system, étendue, a geometric property of light mathematically defined as the product of the area of the light source or entrance pupil and the solid angle into which the light is being emitted from that area, is conserved throughout the system. This invariant leads to compromises between the parameters introduced above, that is, the FOV, the eyebox, the angular resolution, and the device size. For example, if a system is designed to expand the FOV for a given display resolution and pixel size, the eyebox as well as the angular resolution must be reduced, or larger optics would be required. Therefore, careful designs of optical architectures are essential to optimize different parameters simultaneously by managing these types of trade-offs.

For a comfortable user experience, VR/AR devices must be designed in a compact and lightweight form factor, which motivates researchers to attempt to make the optical system as small as possible. For VR NEDs, as see-through properties are not required, the optics used to transmit light from a display panel to the eyes can be relatively simple, often consisting of only a single lens per eye. For a thinner and lighter form factor, Fresnel lenses have been commonly adopted in most modern consumer VR headsets on the market. In addition to reducing the weight and size, lens configurations have been investigated to reduce the distance between the lens and the display without sacrificing the FOV by, for instance, utilizing an optical folding architecture (often called a pancake lens) with polarization-dependent optics,[30,31] a lenslet array (or microlens array),[32,33] or a combination of a lenslet array, optical folding optics, and a Fresnel lens[34] as summarized in **Figure 3**.

For AR headsets and smart glasses, given that the optics must be able to magnify digital contents generated from the display panel and deliver them to the eyes together with real-world scenes, designing optics to reduce the size of the device and increase the FOV at the same time is even more difficult. In this sense, the optical combiner is often considered the most complex and crucial optical element because it dictates the overall image quality, the FOV, and the optical efficiency of the AR NEDs.

Combiners are classified into reflective and diffractive types. Reflective combiners include a multitude of architectures, from curved or freeform half-tone mirrors to birdbath types (with a beam-splitter and a curved mirror), freeform prisms, and cascaded mirrors (**Figure 4**a–d). Reflective combiners typically show optical efficiency of 20–50%, being balanced against transparency and decent imaging without severe chromatic aberrations. However, the size of the optics proportional to the eyebox and the FOV lead to a large form factor. Recently, 2D

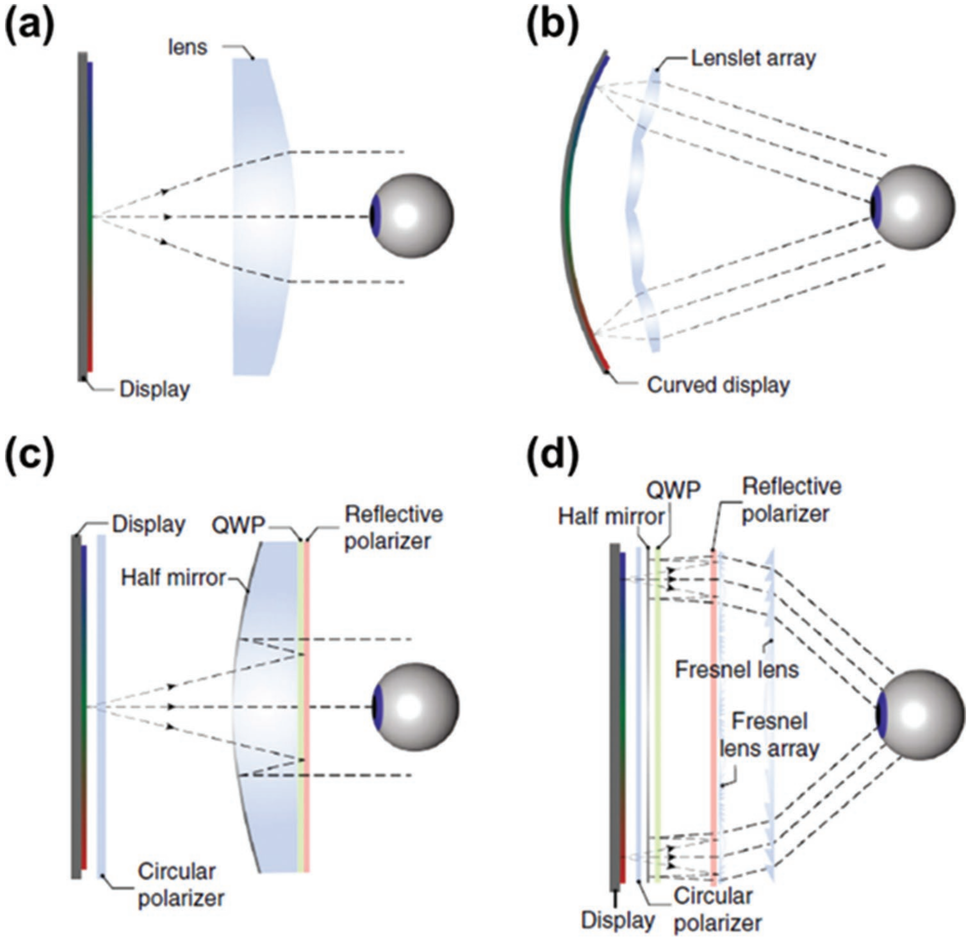

Figure 3. Lens configurations for VR headsets: a) single lens, b) curved lenslet array, c) optical folding type (pancake optics), and d) optical folding type with a lenslet array and a Fresnel lens. Reproduced with permission.[5] Copyright 2021, Springer Nature.

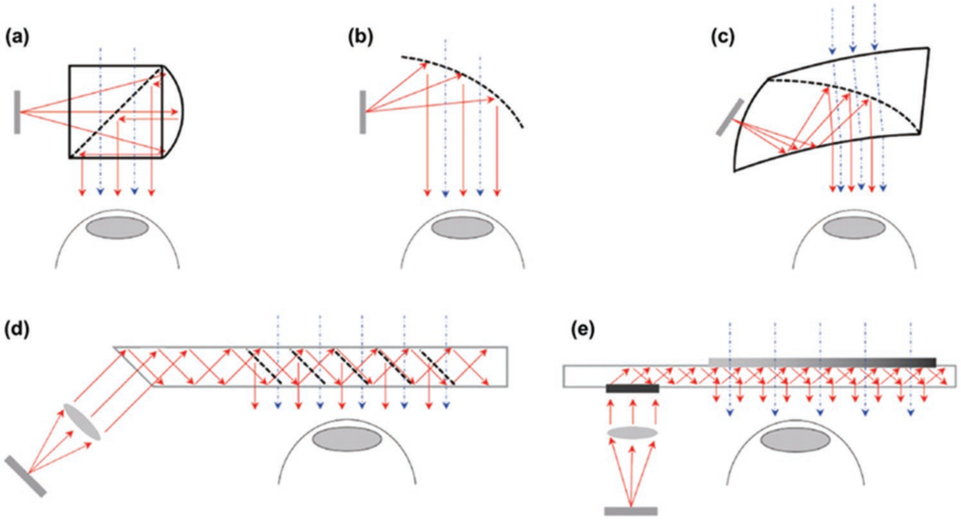

Figure 4. Combiner configurations for AR headsets: a) birdbath type with a beam splitter and a half mirror, b) single freeform half mirror, c) freeform prims, d) reflective waveguide with cascaded partial mirrors, and e) grating-based diffractive waveguide. Reproduced with permission.[248] Copyright 2019, Beijing Zhongke Journal Publishing Co. Ltd.

pupil expansion reflective waveguide combiner technology that allows high color uniformity and optical efficiency exceeding 10% with transmittance of 85% was announced.[35]

Diffractive combiners are typically based on waveguides integrated with a pair of a diffractive grating in-coupler and an out-coupler, and these architectures are particularly useful for AR headsets to enlarge the system étendue without changing the optics thickness (Figure 4e). The major diffractive coupler elements adopted in consumer products are surface relief gratings and holographic volume gratings, where nano-gratings on the surface and the grating patterns of a holographic photopolymer induce the diffraction of incident light, respectively. The basic working principle of diffractive waveguides is as follows: light emitted from each display pixel is collimated and made incident into the in-coupler as plane waves. The incident light is then coupled to the waveguide and trapped by total internal reflection (TIR). This light is guided to the out-coupler, which expands the exit pupil and decouples the light from the waveguide toward the user. Here, the general requirements are to achieve a large FOV, high light output efficiency of the system, and uniformly displayed images. To address these issues, it is commonly required to design in-couplers such that they have high diffraction efficiency and out-couplers to function as a 2D exit-pupil expander for a large system étendue while ensuring outcoupling uniformity over the expanded exit pupil. In addition, both couplers must be tuned for wide angular and spectral bandwidths to provide a decent FOV over a broad spectral range of the display light source. In practice, however, due to the angular and wavelength selectivity of gratings and undesired optical losses from multiple elements, the FOV and light output efficiency are currently limited to around 50° and a few percentage (typically, less than 2%), respectively.[5,36]

Given that a compact and light form factor is in strong demand and light losses in optical systems are inevitable for both VR and AR devices, display technologies that satisfy the specifications for consumer products are also highly essential to develop high-quality VR/AR headsets. In the next section, recent progress in micro-display technologies will be discussed. The reader is referred to more extensive reviews for a more detailed summary in the field of optics for VR/AR headsets.[5,26]

2.3. Display Technology for AR/VR Headsets

Micro-displays, typically less than one inch for AR/VR headsets, can be classified as projection types that require external illumination systems, such as liquid-crystal-on-silicon (LCoS), digital light processing (DLP), and laser-beam scanning (LBS) as well as self-emissive types, such as micro-organic light-emitting diodes (OLEDs) and micro-LEDs.

LCoS is a reflective display in which the incident light is modulated depending on the polarization by controlling LC pixels that are patterned on top of a silicone backplane. LCoS micro-displays have been widely used in the AR/VR industry (e.g., Microsoft HoloLens 1, Magic Leap One) due to their high brightness, good resolution quality, and relatively low manufacturing cost. However, fundamental shortcomings include the limited dynamic range caused by the poor dark state and low optical efficiency due to polarization dependency. DLP controls the reflection of micromirrors to modulate the light amplitude without polarization (cf. DigiLens Design V1). Compared to LCoS, it generally exhibits higher efficiency, as unpolarized light sources can be directly utilized. One common issue associated with LCoS and DLP is that the system size becomes bulky, particularly if LED light sources are employed, hindering their use in compact VR/AR headsets. The LBS system forms 2D images by scanning laser beams with the mirrors of a microelectromechanical system (MEMS) and modulating each pixel (cf. Microsoft HoloLens 2). LBS is often considered to be promising largely due to its small form factor, high contrast ratio, high light efficiency, and high DOF number. However, as the exit pupil of scanning display systems is inherently small, complex compensation optics is required, which leads to high labor and manufacturing costs.

Self-emissive displays based on micro-OLEDs or micro-LEDs have gained much attention mainly due to certain intrinsic compactness compared to LCoS and DLP. Obviously, the key optical parameters reviewed in Section 2.2 necessitate the common requirements of display engines not only for the device size but also for the brightness, resolution, contrast ratio, frame rate, power consumption, and other considerations.

For OLEDs, despite the major examples of success in a wide range of markets from small to large-sized displays, OLED technologies for micro-displays are less mature. High-resolution RGB sub-pixel patterning is one of the critical issues to consider when fabricating full-color OLED micro-displays. Generally, there are two methods of RGB patterning, one of which is directly to deposit individual RGB emission layers in a side-by-side manner using fine metal masks (FMMs) (**Figure 5**a). The other is to make use of white OLEDs with RGB color filters (CFs) (Figure 5b).

For direct patterning, the manufacturing precision of FMMs and accurate alignment to define the RGB areas are extremely

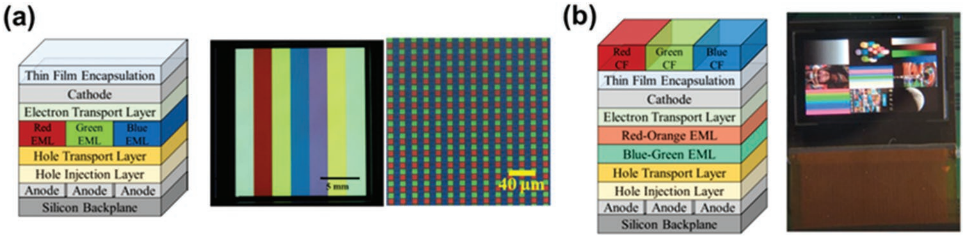

Figure 5. a) Illustration of an OLED stack with directly patterned individual RGB emission layers (left). An example of a directly patterned full-color micro-OLED module and a close-up image of the pixel array (right). b) Illustration of the OLED stack of a white OLED emission layer with RGB color filters (left). An example of the micro-OLED module of a white OLED with color filters (right). (a) Reproduced with permission.[38] Copyright 2017, Wiley-VCH GmbH. (b) Reproduced with permission.[39] Copyright 2019, Beijing Zhongke Journal Publishing Co. Ltd.

important given that the sub-pixels must be structured in a few micrometers. Several studies have demonstrated directly patterned full-color OLED micro-displays with a pixel density exceeding 2600 pixels per inch (PPI) (Figure 5a).[37,38] However, due to the technical hurdles encountered when manufacturing FMMs, drastically scaling down the pixel size even further is challenging.

The strategy of employing white OLEDs with CFs is capable of producing a much higher pixel density, for example, over 5000 PPI (Figure 5b),[39] because the pixel size depends on the area of the CFs and anode pads embedded in the CMOS backplane, both of which are structured by high-resolution lithography technologies. However, the CF array absorbs theoretically >70% of the light emitted from white OLEDs, leading to a reduction in the luminance as well as the power efficiency of OLEDs.[37,40] To compensate for such optical losses, the performance of the white OLED itself must be improved and/or external optics to boost the efficiency is required (e.g., a light-extracting nanostructure[41] or a microlens array[42]).

To date, neither directly patterned RGB OLEDs nor white OLEDs with CFs that achieve high-pixel density levels and high brightness concurrently have been demonstrated. Recently, a novel approach has been proposed based on white OLEDs with metasurface nano-mirrors structured corresponding to RGB sub-pixels, enabling a twofold increase in the luminescence efficiency compared to color-filtered white OLEDs as well as an ultrahigh pixel density of 10 000 PPI (Figure 5c,d).[43] The emission color can be tuned relying on the optical resonance controlled by the shift of the reflection phase of the metasurface mirrors, consisting of nanopillar arrays. Here, the reflection phase is adjusted by patterning the nanopillars with different physical dimensions. To deploy this technology for mass-production, therefore, cost-effective fabrication methods which ensure precise nano-scale patterning yet offer high throughput are strongly required.

In general, a maximum luminance level limited to a few thousand nits is acceptable for direct-view VR applications, but it is most likely not sufficient for AR NEDs, particularly for outdoor use, which requires high luminance, unless the light output efficiency of state-of-the-art combiners is substantially improved. In addition, the broad emission spectrum of a typical OLED is not suitable for the diffractive waveguides of AR devices, which exhibit strong wavelength selectivity.

Micro-LEDs, also as self-emissive devices, share properties similar to those of OLEDs, such as high contrast and fast response time. Due to the intrinsic nature of inorganic materials, however, micro-LEDs show superior performances in term of brightness, efficiency, and durability compared to OLEDs. In the industry, pixelated LED-based displays have been already adopted for ultra-large signage applications and cinema screens, and interest in potential consumer products has grown considerably over the last decade, especially since Sony introduced a 55-in., full-HD micro-LED prototype TV in 2012 and Samsung unveiled a modular 146-in., 4K micro-LED TV in 2018.

In the meantime, micro-LEDs have attracted enormous amounts of attention for small-size displays for wearable devices as well, first from smart watches (e.g., Apple acquired LuxVue in 2014) and later to AR/VR headsets (e.g., Meta (Facebook Oculus) acquired InfiniLED in 2016 and Google acquired Raxium in 2022). Despite such attractive features and the high level of interest, micro-LED technologies still face challenges in high-volume manufacturing with a high production yield. Furthermore, micro-LEDs for micro-displays, although they share the same nomenclature, must meet more rigorous requirements than those for direct-view display panels in many aspects, such as the pixel size, fabrication process, and luminance characteristics, and it is even more challenging to satisfy those demands for full-color display solutions. This is well proven by the fact that only a few products have been announced publicly, limited to smart glasses only based on monochrome micro-LEDs, thus far (e.g., Vuzix Shield, Oppo Air Glass). The major obstacles hindering the manufacturing of micro-LED-based full-color micro-displays are i) efficiency reduction when miniaturizing the micro-LEDs and ii) the integration of individual RGB micro-LED pixels with a drive circuit backplane.

In general, for RGB pixels, green and blue LEDs are fabricated based on InGaN semiconductors grown on a sapphire substrate, in which the emission spectrum is tuned by controlling the composition of each element, whereas state-of-the-art red LEDs are generally based on AlGaInP epitaxial layers on a GaAs substrate for lattice matching. Although several strategies to build an efficient InGaN-based red LED have been introduced recently,[44,45] it is still challenging to achieve decent efficiency comparable to that of blue micro-LEDs. Furthermore, despite the fact that all RGB LEDs can be produced using the InGaN-based chip architecture, no practically feasible technology to vary the composition of elements in quantum wells across a wafer for full-color emission from a single substrate has been demonstrated.[46] One common issue is that as the size of micro-LEDs shrinks, the quantum efficiency drops, leading to low brightness and degradation of the degree of homogeneity. This behavior is primarily attributed to surface defects at the sidewalls acting as non-radiative recombination centers, and the decrease in the quantum efficiency is more severe in AlGaInP-based red LEDs due to the surface recombination velocity and carrier diffusion length being much greater than those of InGaN.[47,48]

To transform bare micro-LED chips to display pixels, the integration process between the micro-LEDs and the electronic driver circuits is essential. For micro-displays in which highly accurate alignment is critical for extremely small pixels (<10 µm), the mass transfer techniques developed for large-scale displays with low PPI (less than a few hundreds) are not suitable. In place of these, monolithic integration methods have been widely investigated. Among them, fully monolithic integration which aims to build both micro-LEDs and to drive thin-film transistors (TFTs) on the same substrate hold great promise with regard to future micro-displays.[49–51] However, the technology is currently in its infancy and thus cannot be directly adapted to consumer products. Compared to fully monolithic approaches, monolithic hybrid integration is more practical. The fundamental idea is to assemble micro-LEDs fabricated on an LED substrate and an Si-based complementary metal-oxide semiconductor (CMOS) backplane by flip-chip or wafer bonding techniques[49,52]; for flip-chip bonding (**Figure 6**a–d), individual micro-LED pixels are structured on the LED substrate and then bonded to corresponding TFTs on the CMOS

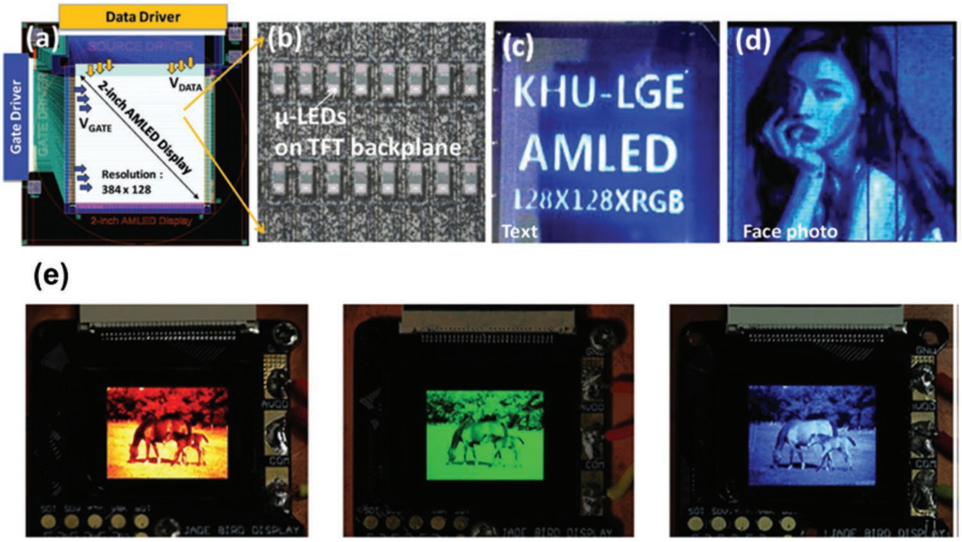

Figure 6. a–d) Two-inch active-matrix micro-LED panel integrated with an oxide TFT backplane using flip-chip bonding. e) 1270 PPI active-matrix micro-LED RGB modules packaged using wafer bonding. (a–d) Reproduced with permission.[54] Copyright 2018, Wiley-VCH GmbH. (e) Reproduced with permission.[56] Copyright 2018, Society for Information Display.

backplane with pixel-wise accurate alignment.[53,54] For wafer bonding (Figure 6e), an entire LED epi-wafer is bonded to the CMOS backplane first, after which micro-LED pixels are isolated directly on the embedded TFTs via high-resolution lithography processes, eliminating the accurate alignment issue and thus allowing a further reduction of the pixel size (<5 μm).[55,56]

Although monolithic integration is promising for fabricating micro-displays with a high pixel density, the most critical drawback is that it is hardly possible to support full-color architectures by transferring or structuring RGB individual pixels due to the nature of the bonding processes. Taking those two major limitations in the efficiency and fabrication process against the decrease in the pixel size into account, leveraging RGB micro-LEDs individually prepared on different substrates is not practically favored for full-color micro-display panels.

Other approaches to realizing RGB full-color micro-LED displays are to utilize color conversion, that is, to down-convert high energy excitation light (e.g., blue or ultraviolet) to light with lower energy (e.g., red or green), by to make use of phosphors or colloidal semiconductor nanocrystals (NCs; including QDs and MHPs). Phosphor-based conversion has several advantages, including a high quantum yield, high luminous efficacy of radiation, high thermal stability, and high chemical/moisture resistance,[57] and it has been widely used to generate white light in applications such as LED lamps, projectors, and LED TVs. The main obstacles when employing phosphors for the micro-display panels of AR/VR devices are that phosphor particles are normally larger than a few micrometers as the light conversion efficiency is inversely proportional to the size of the particles,[48,57] and the light scattering and broad emission spectra from the phosphors are not preferential for diffraction-based optics.

On the other hand, QDs and MHPs are often considered to be promising candidates for color conversion due to the prominent features of a high quantum yield, tunable optical properties depending on the particle size, narrow emission linewidths, and strong absorption in the wavelength range of blue light. To adopt QD (or MHPs) color conversion to full-color micro-displays in consumer markets, it is crucial i) to precisely structure the color conversion layers on each micron-scale subpixel without damaging the underlying LEDs and backplane, ii) to enhance the light conversion efficiency ideally with no leakage of the excitation light, iii) to obtain high color purity with no color crosstalk, iv) to improve the stability of the QD layers for longer lifetimes, and v) to develop manufacturing processes suitable for mass production.

In this regard, the material properties of different classes of QDs and MHPs, cutting-edge studies and core challenges for color conversion and EL, patterning technologies, and future perspectives will be discussed throughout the following chapters.

3. Emerging Nanoscale Emitters for AR/VR Displays

In this chapter, we discuss promising candidate light-emitting materials to improve the color reproduction range of next-generation AR/VR displays. We particularly focus on the optical and structural properties of colloidal inorganic QDs and colloidal perovskite NCs as well as recent advances in their synthesis methods to improve their optical properties and stability.

3.1. Colloidal Quantum Dots (QDs)

Colloidal inorganic QDs are nano-sized compound semiconductor particles exhibiting discrete energy levels and a size-dependent bandgap owing to the quantum size effect that exists when the radius of the QDs is shorter than the exciton Bohr radius.[58–60] As the size of the QDs decreases, the quantum size effect is enhanced and thereby the QDs exhibit a blue-shifted

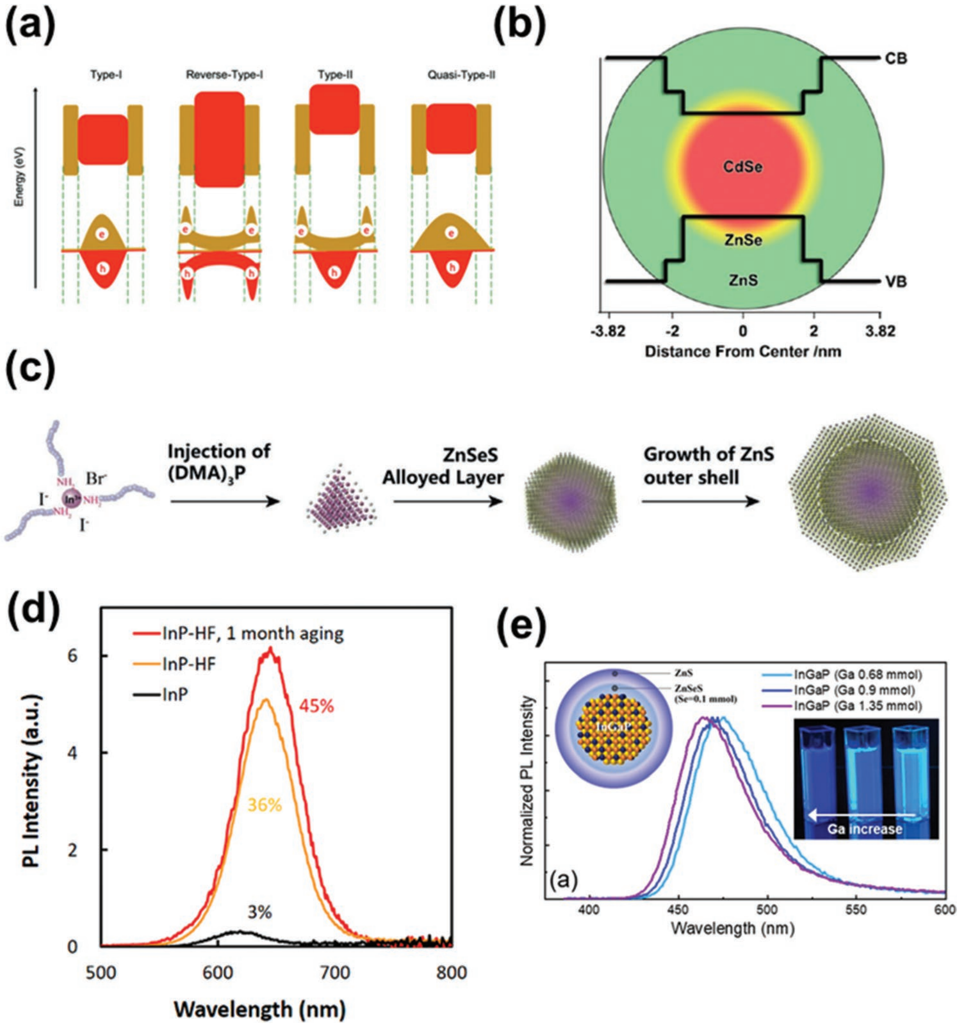

Figure 7. a) Energy level alignment type of core–shell structured QDs. b) Schematic representation of energy alignment in CdSe QD with a multishell structure of CdSe/ZnSe/ZnS. c) Schematic of the InP-based QD synthesis using $(DMA)_3P$. d) PL intensity improvement of InP-based QDs upon HF treatment. e) Effect of Ga doping in InP-based QDs on PL emission. (a) Reproduced with permission.[163] Copyright 2020, Wiley-VCH GmbH. (b) Reproduced with permission.[68] Copyright 2012, American Chemical Society. (c) Reproduced with permission.[81] Copyright 2021, Wiley-VCH GmbH. (d) Reproduced with permission.[84] Copyright 2018, American Chemical Society. (e) Reproduced with permission.[85] Copyright 2020, American Chemical Society.

emission spectrum with an increased bandgap. As a result, depending on their size and composition, QDs show a wide range of emission wavelengths from violet to near-infrared (NIR) with a narrow emission linewidth (typically, full width at half maximum (FWHM) values of 20–30 nm for CdSe-based QDs[61,62] and ≈35 nm for InP-based QDs[63]) and high PLQYs of 80–100%.

3.1.1. Materials' Properties

Due to the large surface-to-volume ratio, QDs are prone to surface defects, such as surface dangling bonds, which can act as nonradiative recombination sites and thereby reduce the PLQY and generate undesirable photophysical phenomena such as blinking.[64] To overcome the problems originating from these surface defects, QDs typically possess a core/shell structure where the surface of the shell is capped with long-chain organic ligands. Core–shell structures can be classified into several different types (e.g., type-I, type-II, inverse type-I, and quasi type-II) according to the alignment of the energy levels (i.e., valence band maximum and conduction band minimum) of the core and shell materials (**Figure 7**a).[65] While the type-I structure assists with the confinement of both electron and hole wavefunctions by shells with a wider bandgap, the type-II structure with a staggered alignment facilitates the transport of a charge carrier (either an electron or a hole), as one charge carrier is confined in the core and the other is confined in the shell. Most QDs employed as color conversion layers (in PL down-conversion displays) and emission layers (in self-emissive QLEDs) have the type-I structure (e.g., CdSe/ZnS), where radiative recombination of holes and electrons can be enhanced.[66] Furthermore, multishell structure is often adopted to reduce the lattice mismatch between core and shell material, for instance, CdSe/CdS/ZnS and CdSe/ZnSe/ZnS (Figure 7b).[67,68]

The core/shell QDs are capped with surface ligands and colloidally dispersed in solvent media. The surface ligands not only passivate the surface defects of the QDs (increasing the PLQY substantially) but also provide long-term colloidal stability in the solvent. The most common combination of a surface ligand and a solvent is a long-chain organic ligand (e.g., alkyl carboxylate, alkyl amines, and alkyl phosphines) and a non-polar solvent (e.g., hexane and toluene). In addition to surface passivation and colloidal stability, surface ligands greatly affect the charge transport properties of the QD films The charge carrier mobility in QD films depends strongly on the length of the ligands, as ligands are mostly insulating.[69] The energy levels of core/shell QDs can also be shifted by surface ligands.[70] Therefore, for both PL down-conversion and EL applications, surface ligands play a crucial role in the fabrication of QD layers with desired optical and electrical properties. Further details and a discussion of the core/shell structure and surface ligands can be found in the literature in other review articles.[6,62,65,71]

3.1.2. Environmentally Benign InP-Based QDs

Despite the high PLQY and narrow emission linewidth, the commercialization of CdSe-based QDs remains limited thus far due to the toxicity of cadmium. As an alternative, environmentally benign InP-based core/shell QDs have been extensively studied owing to the direct bandgap, weak phonon coupling, and small effective charge carrier masses.[72] However, InP QDs are associated with high susceptibility to oxidation.[71] Because both In and P are oxophilic, oxidative defects (e.g., $InPO_x$ or In_2O_3) can easily form during the colloidal synthesis step, considered to be the major cause of the inferior optical properties (i.e., lower PLQY and broader emission spectrum) of InP QDs compared to CdSe QDs.[73] In addition, improving the optical properties of InP QDs often requires a high-temperature synthesis step due to the high covalency of III–V semiconductors.[74,75]

Although the PLQY and emission linewidth of InP-based QDs were far behind those of CdSe-based QDs in the early stage due to their high oxophilicity and high covalency, "high-quality" (i.e., high PLQY ≥ 90%, small FWHM ≤ 35 nm, and a uniform size distribution) InP-based core/shell QDs were able to be achieved with extensive development of synthetic strategies.[24,73,76,77] Such great progress of InP QDs was based on the development of precursors, optimal shell structures, surface ligands, and other synthetic parameters. One of the strategies initially attempted for the synthesis of high-quality InP QDs was to change the reactivity of the P precursor. A two-phosphine approach which introduces highly reactive tris(trimethylsilyl) phosphine ($(TMS)_3P$) and a less reactive triarylsilylphosphine precursor ($P(SiPh_3)_3$) together was attempted in an effort to control the amounts of monomers left for the growth stage.[78] The highly reactive $(TMS)_3P$ contributes to the rapid nucleation upon injection, but a safety issue arises due to its flammability in air. Recently, tris(dimethylamino)phosphine ($(DMA)_3P$) has been used for the synthesis of InP QDs as an alternative phosphine precursor for better safety and cost-effectiveness, showing a moderate reaction speed. However, InP QDs synthesized with $(DMA)_3P$ without compositional engineering of shell showed a lower PLQY of 83% with a larger FWHM (50 nm)[79] than those of InP QDs synthesized using $(TMS)_3P$ (PLQY = 95%, FWHM = 36 nm).[80] The optical properties of InP QDs synthesized using aminophosphine precursors could be enhanced further (PLQY = 95%) by using an inner/outer shell structure (e.g., ZnSeS/ZnS) (Figure 7c).[81] Precise control of the size and uniformity was achieved via a two-step approach using ≈1.9 nm InP QDs as seeds for larger core/shell QDs.[82] Starting from these seeds, the growth of highly monodisperse InP QDs was achieved by the slow and continuous injection of In–P complexes into the seeds, avoiding secondary nucleation.[82] Also, the use of Z-type ligands with strong electronegativity, such as metal halide salts (e.g., $ZnCl_2$, $ZnBr_2$, $InCl_3$) along with conventional long-chain X-type and L-type ligands can enhance the PLQYs of InP QDs by passivating under-coordinated chalcogenides.[83]

State-of-the-art InP/ZnSe/ZnS core/shell QDs show PLQYs of 90–100% and FWHMs of 35–36 nm (for green).[73,80] For instance, the size distribution of green InP/ZnSe/ZnS is enhanced by forming monodisperse InP cores through control of the reactivity between the In and P precursors, which was achieved with an injection of a phosphine precursor at the relatively low temperature of 150 °C, with a subsequent shell-building process at a high temperature. The resulting emission properties resulted in a PLQY of 95% and a FWHM of 36 nm with significantly reduced surface trap states.[80] The PLQY of red InP-based QDs was enhanced by removing the surface trap sites of the InP cores through an additional surface treatment (Figure 7d).[84] A hydrofluoric acid treatment was implemented to obtain an InP core without an oxidative surface, which can act as trap sites, resulting in a PLQY of 98% at 630 nm and a FWHM of 35 nm.[73]

While red and green InP-based QDs show PLQYs that exceeded 90%, blue InP-based QDs still exhibit relatively low PLQYs. The small size of blue InP QDs of less than 2 nm is the main cause of such low PLQYs, as they are more prone to surface defects and have difficulty in synthesizing monodisperse blue core QDs. Precise control over the small InP core size greatly affects the PLQY of blue InP core/shell QDs. For instance, InP QDs ≈1.8 nm in size were achieved by adding the ZnS complex at the early stage of InP growth, suppressing the overgrowth of InP nuclei.[72] With an additional ZnS shell coating, the InP/ZnS core/shell QDs resulted in high PLQYs of ≈52% at 483 nm. Recently, Ga doping was reported as an effective strategy to realize larger pure-blue emissive InP-based QDs with a smaller surface-to-volume ratio and a reduced lattice mismatch of the ZnS shells.[75,85] As the cation exchange procedure of InP is limited due to its strong covalency, synthesis of $In_{1-x}Ga_xP$ QDs typically requires high temperatures above 380 °C.[75] By using a GaI_3-incorporating molten salt as a medium for cation exchange, the pre-synthesized InP was successfully converted to InGaP, finally resulting in the InGaP/ZnSeS/ZnS structure with a reduced lattice mismatch between the InGaP and ZnSeS (Figure 7e).[85] The synthesized QDs exhibited a PLQY of 80% with pure-blue emission at 465nm. However, the FWHMs of the blue InGaP QDs still exceeded 45 nm, indicating a need for further development.[75,85]

The high PLQY of state-of-the-art red and green InP-based QDs may guarantee the successful commercialization of QD color-conversion-based displays in the near future. However, the blue InP QDs should be further developed in both efficiency and stability. For AR devices requiring much higher brightness levels and resolutions than cell phones and laptops, further studies on improving the thermal/photo stability and developing non-destructive high-resolution patterning method for InP QDs are indispensable. The patterning method of colloidal QDs will be further discussed later in Section 4.

3.2. Metal Halide Perovskites (MHPs)

Metal halide perovskites (MHPs) are an emerging class of optoelectronic material attracting significant attention in relation to various applications, such as LEDs, solar cells, photodetectors, and lasing due to their unique optical and electrical properties, featuring high PLQYs, high defect tolerance levels, tunable emission colors in the visible light range, and exceptional color purity and high charge carrier mobility levels.[19,86]

As mentioned in Section 2 above, to exploit a light-emitting material as a color conversion layer or emission layer in AR/VR headsets, the displays of the AR/VR headsets should simultaneously meet the requirements of high luminescence efficiency, excellent color expression (i.e., wide color gamut), high brightness, and a high resolution. Regarding the color gamut, Rec.2020 has been used as a new standard that replaces conventional NTSC standard since 2014, following the development of ultra-high definition display.[87] The comparison of Rec.2020 and other standards such as NTSC, DCI-P3 (for digital camera) is shown in **Figure 8**. Considering the smaller FWHMs (~20 nm) of the emission spectrum of MHPs compared to that of InP-based QDs (≈35 nm), MHP NCs offer great potential with regard to realizing more immersive and realistic AR/VR displays that could satisfy nearly 100% of Rec.2020 in the near future.

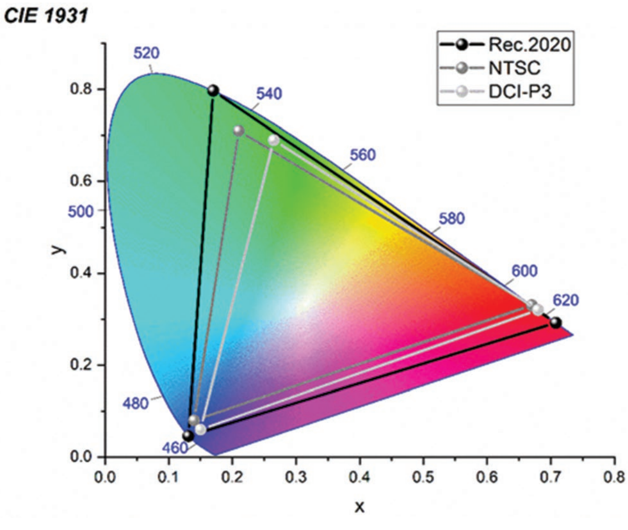

Figure 8. CIE graph showing color gamut standards of NTSC, Rec.2020, DCI-P3.

3.2.1. Material Properties

The basic structure of 3D MHPs is represented as ABX_3, mainly Cs^+, methylammonium ($CH_3NH_3^+$), formamidinium ($CH(NH_2)_2^+$) at the A-site, Pb^{2+} at the B site, and Cl^-, Br^-, I^- at the X site. The B-site metal cations and halide anions form corner-sharing BX_6 octahedra are located at the cubic center; together with the A-site cations, forming an ABX_3 ionic crystal. The Goldschmidt's tolerance factor (t) and the octahedral factor (μ) are two major parameters determining the phase stability of the perovskite crystal structure. The Goldschmidt tolerance factor (t) determines the stability and the extent of distortion of the entire crystal structure, while the octahedral factor (μ) determines the stability of the BX_6 octahedra. They are given as the following equations, where r_A, r_B and r_X represent the radii of A, B, and X, respectively.

$$t = \frac{r_A + r_X}{\sqrt{2(r_B + r_X)}} \tag{1}$$

$$\mu = \frac{r_B}{r_X} \tag{2}$$

The t value greatly affects the crystal structure of MHPs, where the cubic phase is observed when $0.9 < t < 1$, the orthorhombic/rhombohedral phase appears at $0.7 < t < 0.9$, and the hexagonal/tetragonal phase arises at $t > 1$.[20] The BX_6 octahedra of MHPs can be tilted due to the arrangement of A, B, and X ions and the displacement of the ions. The perovskite structure is considered unstable when the μ value is too small or too large. A stable perovskite structure is typically obtained with μ in the range of 0.442–0.895.[88] Because A-site cations of smaller sizes can scarcely maintain the BX_6 octahedron, with μ values of less than 0.4, it becomes impossible to implement a stable perovskite phase regardless of the t value.[89]

MHPs exhibit a direct bandgap that can be readily tuned by controlling the halide moiety (**Figure 9**a). For lead halide perovskites, the energy level structure consists of a valence band mainly depending on halide 5p and a conduction band mainly determined by the spin-orbit coupling characteristic of Pb 6p and halide 5p.[90,91] Therefore, facile control of the emission color is possible by tuning the halide composition. Also, lead halide perovskites have a very high absorption coefficient of $\approx 10^5$ cm^{-1} (cf. $\approx 10^4$ cm^{-1} for GaAs) due to 1) the transitions allowed given the characteristics of the direct bandgap, and 2) a high joint density of states originating from p–p transitions (with a less dispersive lower conduction band compared to GaAs).[20] The strong optical absorption of lead halide perovskites is very useful for color conversion, which will be revisited and discussed in Section 5.

The defect tolerance of MHPs greatly contributes to their exceptional optoelectronic properties. Although MHPs have a high concentration of defects due to their low defect formation energy (0.25–0.39 eV[92]), the defects are mainly localized near the edges of the conduction band and valence band, presenting shallow trap energy levels (Figure 9b).[93,94] For instance, in the case of $MAPbI_3$, defects due to elemental vacancies are located close to the band edges.[91] Although some possible defects (e.g., I_{MA}, I_{Pb}, Pb_i, and Pb_I) exhibit deep transition levels between the bandgaps, such defects have high formation energy, causing the

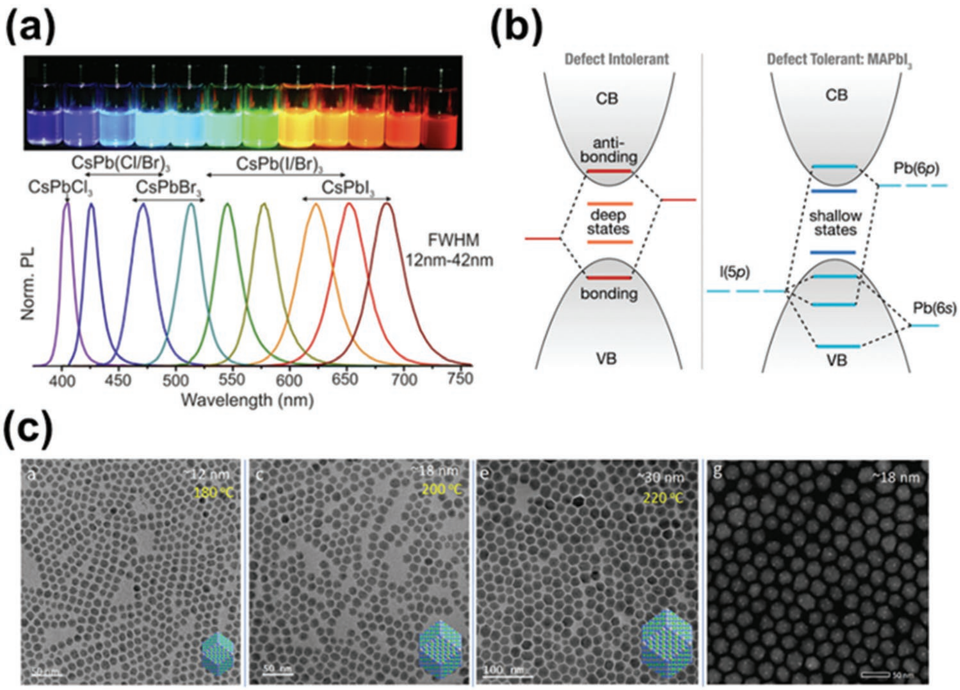

Figure 9. a) PL emission spectrum of various MHPs. b) Defect-tolerant properties of MHPs. c) Different shape of MHP NCs synthesized by tuning the temperature during hot injection method. (a) Reproduced with permission.[97] Copyright 2017, American Chemical Society. (b) Reproduced with permission.[94] Copyright 2017, American Chemical Society. (c) Reproduced with permission.[108] Copyright 2020, American Chemical Society.

dominant defects of MAPbI_3 to be composed of only shallow trap sites. As a result, the defect-tolerance properties contribute to the significantly low nonradiative recombination rates in bulk perovskite films with high trap site densities.[95]

MHP emitters can be largely divided into two types: bulk polycrystalline films and colloidal NCs.[96] The bulk thin film and the NC types mainly differ in terms of their nucleation and growth mechanisms. In colloidal MHP NCs, crystallization occurs during colloidal synthesis by rapid nucleation and limited growth in a solution. Nucleation is typically initiated by an injection of an AX precursor solution (e.g., CsBr) into a flask (or vial) of BX_2 precursor solutions (e.g., PbBr_2), forming colloidal ABX_3 NCs capped with organic ligands. For bulk polycrystalline films, crystallization occurs during the spin-coating of an ABX_3 precursor solution (e.g., MABr and PbBr_2 precursors dissolved in dimethyl sulfoxide). This indicates that crystallization and deposition are separate processes in colloidal MHP NCs but that they occur simultaneously in MHP polycrystalline films. Among the two types, colloidal MHP NCs generally show higher PLQYs owing to the exciton confinement effect.[97,98] Unlike conventional QDs, the emission wavelength and linewidth of MHP NCs are independent of the corresponding particle sizes, as the electronic band structure of MHP NCs is determined only by the composition and crystal structure of the MHPs (assuming that the size of the NC exceeds the corresponding exciton Bohr diameter; that is, in the absence of a quantum size effect), while the electronic band structure of QDs depends on their size.[99,100] Thus far, all red, green, and blue MHP NCs exhibit near-unity PLQYs and small FWHMs (<20 nm for green and <30 nm for red) with effective defect passivation strategies.[101] In contrast, MHP polycrystalline films typically show comparatively lower PLQYs[102,103] than those of MHP NCs. Also, the optical and electrical properties of MHP polycrystalline films strongly depend on the deposition process (often accompanied with an anti-solvent treatment during the spin-coating step) and the resultant grain packing structure,[99,104] leading to large fluctuations in the optical/electrical properties, especially for large-area devices. Considering the higher PLQYs of colloidal MHP NCs and the fundamental limitation of MHP polycrystalline films, colloidal MHP NCs are most likely the appropriate emitter type for use as a color conversion layer in next-generation AR/VR displays.

Regardless of the emitter type, the low stability of MHPs limits the commercialization of MHP-based optoelectronic devices and displays.[105] In Section 3.2.2, we discuss various strategies used to improve the stability of colloidal MHP NCs; in this case purification, defect passivation, surface ligand control, and doping.

3.2.2. Improving the Stability of Colloidal MHP Nanocrystals

For a better understanding of stability improvement strategies, first we briefly review representative synthesis methods of colloidal MHP NCs. The synthesis methods of MHP NCs are mainly classified into two types: hot injection and ligand-assisted reprecipitation (LARP). The hot injection process often includes the injection of an A-site cation precursor into a BX_2 solution with non-coordinating solvents at elevated temperatures. The precursor solutions used often include various types of ligands to provide colloidal stability and control the morphology of the NCs. The nucleation and growth process occurs immediately after the rapid injection of the A-site cation precursor solution. As the reaction is completed within a short time (typically <60 s) by a subsequent quenching process, colloidal MHP NCs with high uniformity are synthesized.[19] Due to the relatively low solubility of CsBr in dimethyl formamide and dimethyl sulfoxide (commonly used solvents for perovskite precursors), the hot injection method is mainly used to synthesize inorganic MHP NCs. Many researchers have focused on improving the PLQYs and the colloidal stability of $CsPbBr_3$ NCs and on controlling the size/shape of the NCs by adjusting the reaction variables (e.g., reaction temperature, duration, the type/ratio/concentration of precursors).[97,106–108] Recently, orthorhombic $CsPbBr_3$ NCs with 12 facets were synthesized by utilizing α-halo ketone forming tertiary ammonium ions, while six-faceted NCs have resulted from primary ammonium ions (Figure 9c).[108] The 12-faceted $CsPbBr_3$ NCs show near-unity PLQYs with high colloidal and phase stability levels. However, the hot injection method is somewhat limited in terms of scalability given that the rapid temperature drop at the point of the injection would be enhanced with a large amount of precursor solution, leading to the inhomogeneous nucleation/growth of NCs, a concomitant broad size distribution and reduced PLQYs.

In comparison with the hot injection method, the LARP method has its advantages in terms of simplicity and scalability. Typically, the precursor solution with AX, BX_2, and ligands in polar solvents (typically, DMF) is dropped into a non-polar solvent while stirring the mixture at room temperature. Owing to the significant change in the solubility upon the addition of the precursor solution, colloidal MHP NCs form instantaneously. The sizes of MHP NCs can be tuned by controlling the amount and chain length of the organic ligands.[100,109] However, an inherent drawback of the LARP method is that the inevitable use of DMF can decompose the MHP NCs, as MHPs are soluble in DMF.

The stability of as-synthesized MHP NCs can be enhanced by a subsequent purification process using anti-solvents. Because the density of the ligands greatly affects the stability and quality of the NCs, the purpose of purification is to extract excess ligands and impurities through centrifugation. An insufficient amount of ligands will result in a MHP NC surface with a high defect density level, while an excessive amount of ligands will deteriorate the use of NCs in devices due to the insulating characteristic of ligands. Effective purification will lead to the adequate passivation of under-coordinated atoms and trap sites at the surface, which can serve as nonradiative recombination paths upon ligand loss. The extent of purification and surface passivation can be tuned by varying the anti-solvent volume ratio, the centrifuge speed, and the time. Methyl acetate, ethyl acetate, acetone, acetonitrile, 1-butanol, and methanol can be used as anti-solvents to precipitate MHP NCs dispersed in toluene. The extent of precipitation differs according to the chain length and polarity of the anti-solvents used.[110] Using ligands with higher affinity can lead to better surface-passivated MHP NCs by preventing the excessive detachment of ligands upon purification.[111]

To overcome the low stability issue, various synthesis conditions are adjusted to prevent the formation of surface defects, which are critical to the overall stability of MHP NCs due to the high surface-volume ratio. Surface defects of MHP include under-coordinated Pb^{2+} and halide vacancies. The most widely known experimental method for solving the halide vacancy issue is synthesis under a halide-rich condition. In most MHP NC synthesis processes, metal halide (BX_2) serves as the precursor for both B-site cations and the X-site anions, which is an obstacle in controlling the precise control of stoichiometry. For precise control of the stoichiometry, a three-precursor method, using different precursors for each A, B, and X ion, was suggested as a possible strategy by which to minimize the generation of halide vacancies.[112,113] Using the three-precursor method is advantageous in providing halide-rich environment, which is a promising synthesis adjustment for suppressing halide vacancies. In addition, the surface termination of halide perovskite greatly affects the stability of MHP NCs.[114] For instance, the use of *N*-bromosuccinimide or benzoyl bromide assisted the efficient protonation of oleylamine, resulting in MHP NCs with lead-halide-terminated surface showing enhanced stability.[112,115] Additives can affect the growth of the MHP crystal plane as well as the surface termination. Incorporating $ZnBr_2$ induces stable (100) surface passivation with low formation energy, which results in highly stable MHP NCs due to the inhibited formation of unstable (100) surface.[116]

Differing types of ligands also contribute to further improvements of the stability of MHP NCs.[117] In MHP NCs, a ligand not only prevents agglomeration but also serves to fill the surface defects. Moreover, given that ligands are labile in a colloidal state, ligands that strongly bind to the surface will result in improved stability. For instance, zwitterionic ions, sulfonate, and phosphate ligands have been introduced for effective surface passivation.[118–120] Specifically, phosphate ligands show improved resistance against an ambient atmosphere with a strong affinity toward Pb^{2+} ions.[121] Branched ligands such as polyethyleneimine can result in minimized Br^- vacancies along with improved stability by providing a strong steric effect.[81] Similar to QDs, the synthesis of core-shell MHPs is also being studied to achieve stabilized MHP NCs. For instance, $FAPbBr_3$ was found to retain ≈80% of its initial PLQY after 70 days with an effective passivation of surface defects by epitaxially grown $CsPbBr_3$ shell.[122,123]

Metal ion doping is a strategy that can precisely tune the properties of MHP NCs.[124] Various ions, such as lanthanides and transition metals, are used as dopants. This doping strategy not only increases the thermal/phase stability but also affects optical electrical properties, such as the PLQY, the n- and p-type properties, and the electronic band structure.[125] Among various factors, the size of the dopant can increase the phase stability by influencing the lattice structure. Nd^{3+} with an ionic radius of 0.98 Å replaces Pb^{2+} (≈1.19 Å) when doped to $CsPbBr_3$, resulting in increased air/thermal stability owing to the increased tolerance factor.[126] Moreover, vacancy formation can be inhibited through doping. Ni^{2+} doping in lead MHP leads to an increase in the formation energy of Pb and halide vacancies, with a PLQY of more than ≈63% in water, while pristine $CsPbBr_3$ undergoes complete degradation to a colorless solution.[127] Doping of Ni^{2+} into pristine $CsPbBr_3$ was also reported to increase the stability, which shows a negligible decrease in the PL intensity upon 48 h (**Figure 10**a).[128]

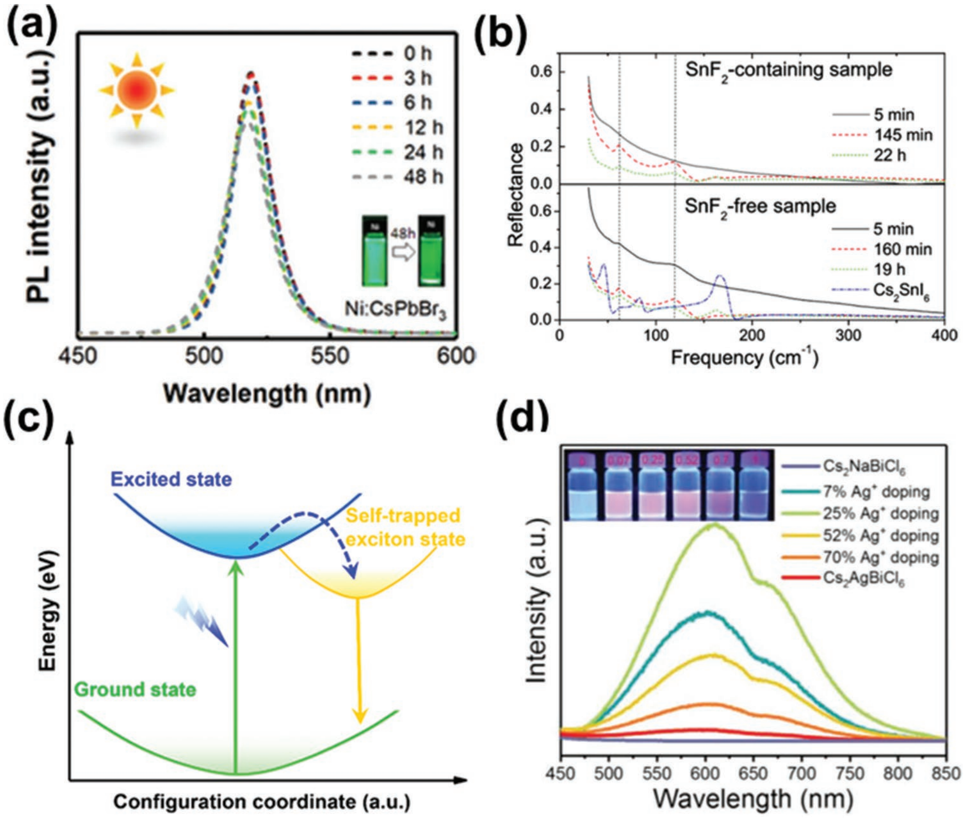

Figure 10. a) Enhanced stability of $CsPbBr_3$ NCs through Ni doping. b) Evolution of the FIR spectra for SnF_2-free and SnF_2-containing $CsSnI_3$ samples after exposure to an ambient condition. c) Schematic representation of self-trapped exciton emission. d) Broad PL emission spectra of lead-free double perovskites. (a) Reproduced with permission.[127] Copyright 2021, Wiley-VCH GmbH. (b) Reproduced with permission.[133] Copyright 2017, American Chemical Society. (c) Reproduced with permission.[142] Copyright 2020, American Chemical Society. (d) Reproduced with permission.[145] Copyright 2020, Wiley-VCH GmbH.

3.2.3. Environmentally Benign MHPs

The toxicity of lead is another primary obstacle to the commercialization of MHP, along with the stability issue. The US EPA stipulates that the contents of Pb^{2+} ions in air and water should be lower than 0.15 and 15 μg L^{-1}, respectively.[128,129] Further, Pb waste over 5 mg L^{-1} is considered hazardous, implying the need for controlled regulation. However, the excellent optoelectronic properties of current MHP NCs are highly dependent on lead-based MHP.[130] Although only a small amount of lead is expected to be observed in MHP displays, continuous attempts to replace lead with other eco-friendly elements are being conducted. However, the properties and stability have not yet reached those of lead-based MHPs.

In the early stage, Sn^{2+} and Ge^{2+}, with ionic radii and charges similar to Pb^{2+} were considered the most probable candidate to replace lead while preserving the 3D cubic structure of the perovskite. In the case of Sn^{2+}, $5s^2$ electrons form an antibonding valence band maximum and contribute to a stabilized conduction band minimum. However, the most serious drawback associated with both Sn^{2+} and Ge^{2+} is that they are prone to oxidization. For instance, the perovskite structure changes to A_2SnX_6 as Sn^{2+} oxidizes to Sn^{4+}, resulting in a modified double-perovskite structure. Reducing agents such as H_3PO_2 have been incorporated to prevent oxidation. The H_3PO_2 prevents a pathway to Sn^{4+} by inhibiting the formation of SnI_4, eventually leading to an enhancement in the PLQY, which reaches 1.35% without being oxidized to A_2SnX_6.[131] Naphthol sulfonic acid has both a Lewis-base sulfonic group and a hydroxyl group, allowing it to passivate dangling Sn^{2+} bonds while providing a reducing atmosphere to prevent Sn oxidation.[132] In addition, the incorporation of excess Sn source (e.g., SnF_2) is one of the most promising strategies to prevent the oxidation, along with suppressing the generation of under-coordinated Sn^{2+} which is considered as a main reason for PL quenching in Sn perovskites (Figure 10b). Unlike the A-site cation and halide ion vacancy, under-coordinated Sn^{2+} acts as a deep trap site and thus affects non-radiative emissions. The incorporation of tin halides, including SnF_2 and SnI_2, allows them to act as an additional Sn source to compensate for the Sn vacancies while also passivating surface halide vacancies.[133] However, the highest PLQY reported for Sn-based perovskite is only 18.4% even when the synthesis step is performed under a halide-rich condition.[134]

Recently, another 3D cubic perovskite candidate emerged. With low toxicity and a similar ionic radius, bivalent lanthanide ions are among the most promising candidates to replace lead without sacrificing its excellent optical properties.[135] Lanthanide ions were primarily introduced into perovskites as doping agents assisting the multi-functionality of MHPs.[136]

Specifically, europium ions have drawn much attention by researchers seeking to realize pure blue emission, which is rarely reported even for lead MHPs. Europium-based perovskites possess deep-blue emissions of around 440 nm owing to the 5d–4f transition. Lanthanide ions can have both 2+ and 3+, but 2+ ions must be used to form a 3D perovskite structure. However, due to the oxophilic nature of the 2+ ion, it is difficult to utilize the 2+ ion as a main ion which participate in the solution-based synthesis. The highest values reported thus far are a PLQY of ≈2% and a FWHM ≈19 nm for $CsEuCl_3$, which shows insufficient optical characteristics, limiting the utilization of europium and lanthanide perovskites.[137]

Additionally, lead could be replaced by heterovalent metal ions. Most replacement efforts with heterovalent ions result in structural distortions, leading to perovskite-derived structures with reduced dimensions. Among heterovalent candidates, Sb^{3+} and Bi^{3+} are most frequently used as candidates to achieve the $A_3(Sb \text{ or } Bi)_2X_9$ structure, which results in a low-dimensional perovskite including a 0D dimer phase and a 2D layered structure. In particular, Bi^{3+} exhibits a $6s^2 6p^0$ electronic configuration identical to that of Pb^{2+}. It has a higher PLQY value than Sn^{2+} and Ge^{2+}-based MHPs and also has higher thermal and photostability due to its defect-tolerant characteristics. Nevertheless, the reported maximum PLQY is insufficient to meet optical requirements of commercial displays. Further, the broad PL peak (typically over 50 nm), which is a typical feature for low-dimensional perovskites due to self-trapped excitons (STEs), is the most significant limitation (Figure 10c).[90] Although $M_3Sb_2I_9$ (M = Cs^+, Rb^+) has shown much enhanced FWHM of ~30 nm, the PLQY values were significantly lower than the lead-based MHPs due to the trap sites within the bandgap.[138] The highest reported PLQY value for $Cs_3Sb_2Br_9$ is approximately 50%, which is insufficient for commercialization.[139]

Copper has been another promising material to replace lead due to its electronic charge, low toxicity, and price advantages. Cu was initially incorporated as a dopant for Pb-based MHPs to stabilize the cubic phase.[140] For typical Cu-based perovskites with the A_2CuX_4 structure, the narrowest FWHM reached 68 nm, with a PLQY of ≈51% for Cs_2CuCl_4. Despite the broad FWHM and limited PLQY value, the typical Cu-based perovskites are advantageous in terms of stability.[141] Recently, the 0D copper-based perovskite Cs_3CuI_5 NC reached a record T_{50} value of ≈108 h, which may be attributed to the suppressed diffusion of Cu vacancies. Although the 0D Cs_3CuI_5 NC reached an absolute PLQY of ≈87%, further improvement in the surface roughness is required before being applied to actual devices.[142]

The mixture of heterovalent ions (3+ and 1+) typically results in double-perovskite structures ($A_2(M^{3+}M^{+})X_6$), such as $Cs_2AgBiCl_6$ and $Cs_2AgInCl_6$.[143] The double perovskite is also associated with a large Stokes shift and greatly expanded FWHM, typically over 100 nm, despite possessing strongly guaranteed stability with better exciton recombinations owing to the larger exciton binding energy levels (Figure 10d). Thus far, double perovskites are often not appropriate for optoelectronic performances due to the broadening of the emission peak, which is attributed to the emission in the self-trapped state, along with the low PLQY, peak broadening, a large bandgap, and parity-forbidden transitions due to surface defects.[144] To overcome such issues, doping is the most commonly used strategy to offset the shortcomings of double perovskites. Among them, it has been reported that the introduction of Mn^{2+} greatly affects increased PLQY outcomes by, for instance, the effect of an additional energy transfer channel. For instance, while pristine $Cs_2AgBiCl_6$ NCs show a relatively low PLQY of <5% with a wide FWHM over 100 nm,[145] co-doping of Na^+ and Mn^{2+} in $Cs_2AgBiCl_6$ result in a significantly enlarged PLQY of 45% as Na^+ ions assisted a higher density of state of STEs and Mn^{2+} ions exhibited a distinct energy transfer process to self-trapped emissions.[146] However, the orange shift of the emission peak due to the doping of Mn^{2+} is still a problem to be solved. Doping with monovalent and trivalent ions was also reported to increase the PLQY of double perovskites by ≈22% for $Cs_2Ag_{1-x}Na_xInCl_6$ in Na-rich conditions, as both Bi^{3+} and Ag^+ contributes to the rise to localized energy levels.[147] In relation to this, Na alloying also positively contributed to the enhancement of the PLQY by breaking the parity forbidden by the changing wavefunction symmetry of STEs but exhibiting a broad FWHM exceeding 100 nm.[148] Recently, it has also been demonstrated that lanthanide ion doping for Bi:$Cs_2AgInCl_6$ can lead to PLQYs of over 40% due to the extra Ln^{3+} emission, still not rectifying the narrow FWHM issue, however.[149]

4. Patterning Technology for Nanoscale Emitters

For an immersive AR/VR experience by users, the resolution is one of the most important features in AR/VR displays.[150] Higher pixel density levels provide better resolutions, leading to finer details and thereby delivering a more realistic image to users. Considering that most AR/VR devices are wearable and have small display panel sizes (typically, 1–2 in. for smart glasses), a small pixel size is required to achieve a high resolution.[151] The pixel size of high-resolution AR/VR applications should be reduced to a few µm or less to prevent screen blurring, pixelation, and the screen door effect, which may occur at low pixel density levels (less than ≈500 PPI).[152–154] Due to the angle-dependent display hardware with a greatly shortened viewing distance, the term 'PPD' is more relevant rather than the widely used 'PPI' in the field of AR/VR displays.[155] Currently, the resolution required for the commercialization of AR/VR displays is known to be 60 PPD, which is correlated with the resolving power of 20/20 vision of human eyes.[5] As mentioned in Section 2.2, the recent trend in AR/VR device fabrication is to reduce the display module as small as possible for a slim form factor, while retaining the FOV of the optical system larger than the practical requirement (i.e., $FOV_{VR} > 100°$, $FOV_{AR} > 45°$).

Therefore, high-resolution patterning methods of light sources and color-converting nanomaterials must be developed to realize such high resolutions. As mentioned earlier, the next-generation displays are most likely going to adopt display panels incorporating colloidal QDs (or MHPs) as color filters or EL emission layers. Because the implementation of a full-color array with R, G, and B subpixels is necessary in both cases, advances in patterning technology are significant.[156] The patterning of color-converting nanomaterials requires optimization of various attributes, for example, the resolution, throughput, fidelity, and uniformity, without sacrificing the luminescent properties of the nanomaterials.[157] In addition, orthogonal processing is essential to minimize the damage on the underlying layers, especially considering the consecutive patterning of multi-color array devices. Conventionally used patterning methods include photolithography, inkjet printing, and nano-imprinting. However, in order for such methods to be applied to 'solution-processable' color-converting nanomaterials and ultimately implemented in AR/VR NEDs, there are several problems to be solved. For instance, the deposition of QD solutions onto pre-patterned substrates may lead to the formation of nonuniform patterns due to the capillary action.[158] The pattern nonuniformity can also originate from PR swelling and coffee-ring effect.[159] Also, the PR development process may impair the structural and optical properties of QD patterns.[157,160] In addition, physically transferring the patterns through elastomeric stamps may result in limited fidelity and throughput. Therefore, further studies on high-resolution patterning technology for color-converting nanomaterials should be proceeded.

In this chapter, we discuss various patterning techniques for colloidal QDs and MHP NCs, focusing on recent strategies to overcome the aforementioned limitations (**Figure 11**).

4.1. Conventional Photolithography

Photolithography is the most widely used patterning technique in the display industry. The basic photolithography process is performed using a photoresist (PR) and includes the following steps: 1) PR spin-coating on a bare substrate, 2) prebaking of the PR, 3) alignment and exposure to a light source (e.g., deep UV at 254 nm), 4) post-exposure baking, 5) the development of PR patterns, 6) the deposition of target materials, and 7) the PR lift-off process.[157] With photolithography, a uniform high-resolution pattern on a large-area substrate can be easily fabricated with high throughput and reproducibility.[161] However, the application of photolithography has been limited in colloidal emissive NCs for the aforementioned reasons such as PLQY loss and nonuniformity.[7] In addition, for MHPs, the use of PR developers, which are typically based on polar solvents, can cause severe damage to the MHP patterns due to the MHP's ionic characteristics.

Various methods have been proposed to minimize the deterioration of the luminescence properties of the emissive layers during the photolithography process. The use of sacrificial passivation layers is one of the most promising methods to prevent damage to the emission layers, such as the uneven line edges which often occur during the lift-off process.[162] For instance, poly (methyl methacrylate) (PMMA) can be utilized as a passivation layer to prevent solvent-related damage of the MHP layer (**Figure 12**a).[163] The degradation of emission layer during development process was minimized as the PMMA protection layer was etched instead of the perovskite layer, thereby retaining ≈70% of the initial PLQY with a clear ≈3 µm pattern. On the other hand, parylene-C with low permeability to solvents, worked as an intermediate layer which can be peeled-off mechanically by a tweezer.[162] The ≈2.5 µm thick parylene-C layer deposited underneath the perovskite layer enables the dry-lift off process, which results in the complete prevention of the dissolution problem. Hence, nearly 90% of PLQY was preserved even after multi-color patterning (Figure 12b,c).

Providing orthogonality between the emission layers and PR solvents (i.e., enhancing solvent resistance of the emission layers) is another effective strategy to prevent the dissolution and damage of the emissive layers during the photolithography process. The stability of CdSe and InP QDs can be enhanced by

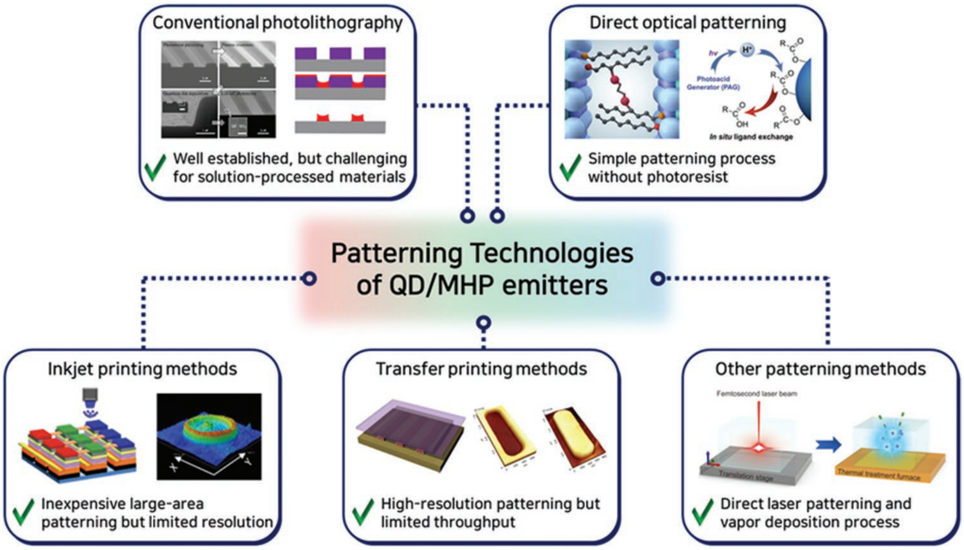

Figure 11. Overview of the patterning processes used for the QD/MHP emitters (Conventional photolithography) Reproduced with permission.[249] Copyright 2016, American Chemical Society. (Direct optical patterning) (Left) Reproduced with permission.[190] Copyright 2022, American Association for the Advancement of Science. (Right) Reproduced with permission.[157] Copyright 2020, Wiley-VCH GmbH. (Inkjet printing methods) (Left) Reproduced with permission.[250] Copyright 2020, American Chemical Society. (Right) Reproduced with permission.[171] Copyright 2016, American Chemical Society. (Transfer printing methods) Reproduced with permission.[178] Copyright 2020, Springer Nature. (Other patterning methods) Reproduced with permission.[180] Copyright 2020, American Chemical Society.

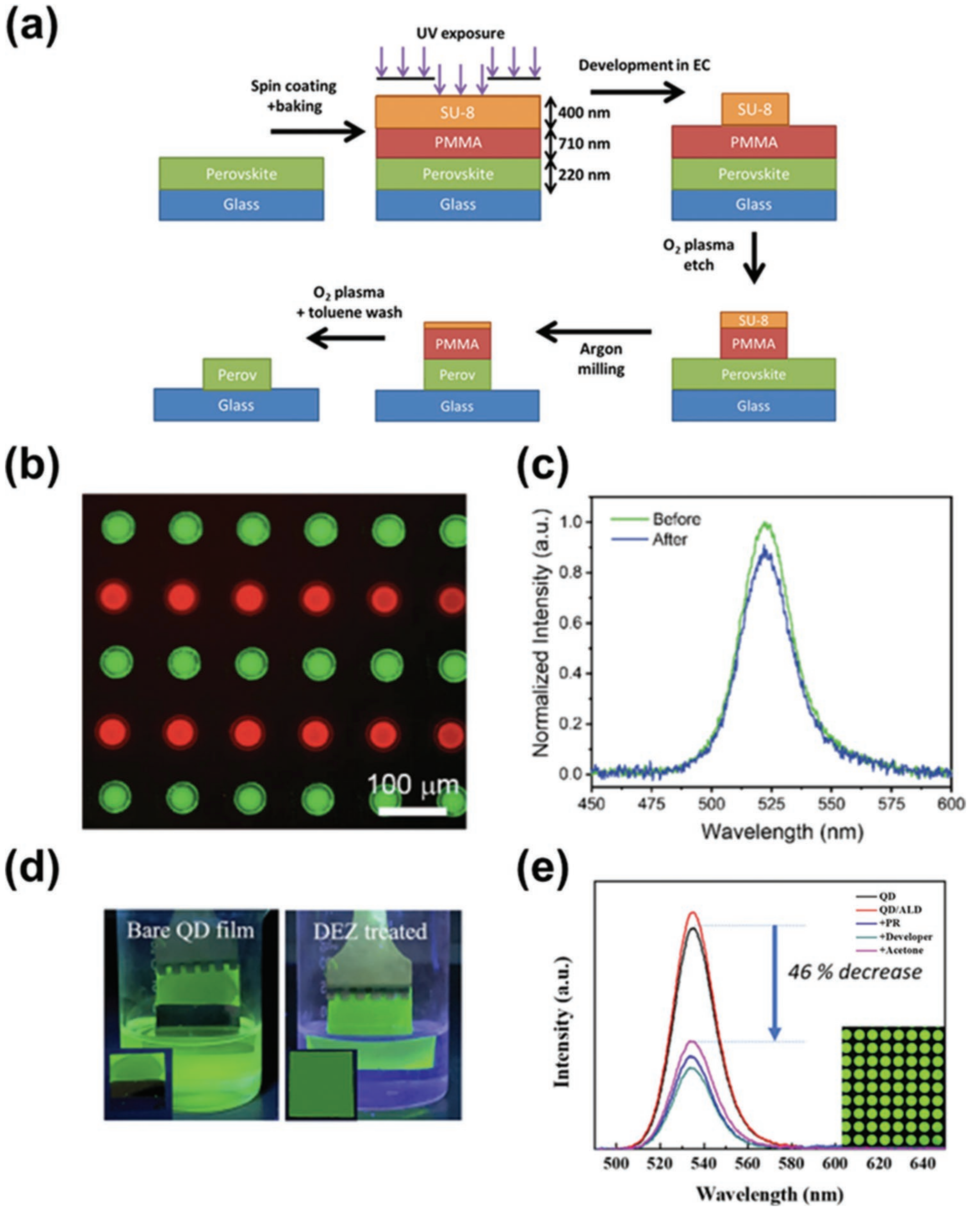

Figure 12. a) Schematic procedure of the patterning process with a PMMA sacrificial layer. b) Multi-color MHP patterns achieved through dry lift process. c) PLQY drop of green MHP after the multi-color patterning process. d) Photographs of bare QD film and DEZ-treated film. e) PL intensity drop upon each patterning procedure. (a) Reproduced with permission.[163] Copyright 2018, American Chemical Society. (b, c) Reproduced with permission.[162] Copyright 2020, American Chemical Society. (d, e) Reproduced with permission.[164] Copyright 2021, American Chemical Society.

atomic layer deposition of diethylzinc (DEZ), which works as an additional capping agent for defects that are not passivated by ligands (Figure 12d,e).[164] Due to the enhanced stability of the films, a direct PR coating right on the top of the QD layer was possible without deteriorating the emissive layer during lift-off process. In addition, the use of a fluorinated stripper was reported as a promising method for providing the orthogonality to MHPs.[165] $CsPbBr_3$ NCs were deposited on a photoresist pattern upon a fluorinated polymer and subsequently the development process was proceeded by using fluorinated stripper, which shows minimal interaction with MHPs.[166] As a result of the minimized dissolution and deterioration of MHP NCs, the emissive multi-color MHP patterns of 1,000 PPI were demonstrated.

Although high-resolution pixels may be realized through photolithography, advanced patterning process which is capable of avoiding direct damage on the emitter patterns and thus mitigating the PLQY drop should be further developed. For instance, although the additional protection layers prevent emitter patterns from being exposed to harsh environments such as developers containing polar solvents, the consecutive deposition and lift-off processes of the protection layers inevitably require extra steps in the case of multi-color patterning, which restricts throughput in mass production. In this respect,

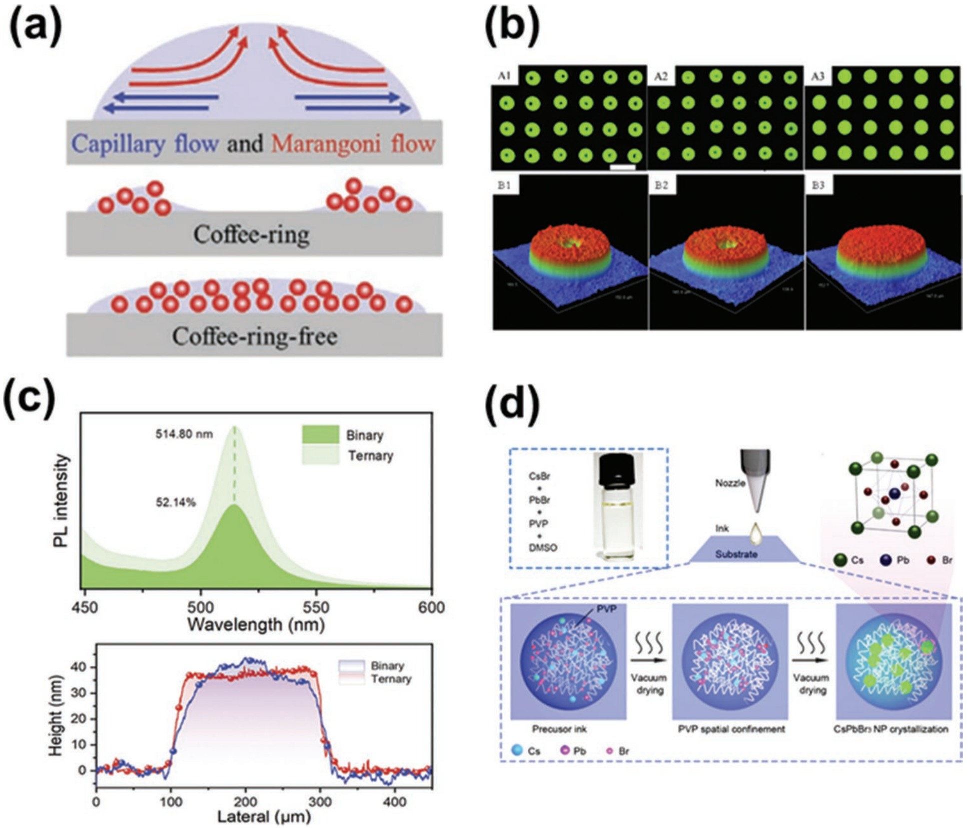

Figure 13. a) Schematic diagram of the pattern morphology upon inkjet printing, with and without the coffee-ring effect. b) PL microscopic and 3D morphology images of mixed solvents with different volume ratios (1,2-dicholorobenzene in cyclohexylbenzene). c) Enhancement of the pattern uniformity and PLQY by using ternary precursors. d) Schematic of inkjet printing procedure of MHP with PVP. (a) Reproduced with permission.[169] Copyright 2020, Wiley-VCH GmbH. (b) Reproduced with permission.[171] Copyright 2016, American Chemical Society. (c) Reproduced with permission.[172] Copyright 2022, Wiley-VCH GmbH. (d) Reproduced with permission.[173] Copyright 2019, American Chemical Society.

the development of PR strippers with complete orthogonality may be a promising path forward.

4.2. Inkjet Printing Methods

Inkjet printing is a non-contact patterning method that can be applied to large-area patterning without the need of a mask, which provides high design flexibility. Due to the drop-on-demand feature, i.e., droplets ejected from a nozzle are exclusively patterned on desired positions, the inkjet printing method is widely utilized as a cost-effective patterning technology. However, the use of this method for small-sized, high-resolution NED displays has been limited so far due to the relatively low available resolution (approximately a few tens of micrometers) and low pattern uniformity. Electrohydrodynamic (EHD) printing has thus been introduced as an approach similar to inkjet printing to overcome these limitations. In EHD printing, tangential force is applied to the ink surface by an electric field, in which the meniscus is transformed into a Taylor cone shape, resulting in small-sized droplets (sub-µm scale) that form a pattern.[167,168] The EHD printing can provide a very high resolution (ultimately up to ≈50 nm) with versatility in terms of printing materials and solvent viscosity levels.[167,169]

To generate a uniform high-resolution pattern by inkjet printing, precise and small patterns with high reliability should be achieved.[170] The fluid properties of the ink are the most important factors to realize such patterns. In particular, the viscosity, pH value, and boiling point of the solvent used should be optimized to induce appropriate control between the outward capillary flow and inward Marangoni flow in the droplets. In this sense, suitable solvent selection is significant to reduce coffee ring effect, which occurs due to the difference in the evaporation rate inside the droplet, and thus result in a uniform film morphology (**Figure 13**a).[169]

Various mixed-solvent strategies have been studied to obtain desired solvent properties. For instance, a 20 vol% of 1,2-dicholorobenzene in cyclohexylbenzene was used as an ink solvent for the patterning of CdSe/ZnS/ZnS QDs (Figure 13b).[171] Due to the reduced surface tension upon the addition of 1,2-dicholorbenzene, the higher solvent evaporation rate resulted in the suppression of the coffee-ring effect. The mixed-solvent method can also assist the inkjet printing of MHPs but the choice of solvents is limited. Certain solvents are not suitable in MHP inks; polar solvents might dissolve MHPs due to their ionic bonding nature, and the use of conventional inkjet printing solvents (e.g., ether, ketone, and haloalkanes) might precipitate MHP NCs. Specifically, the use of a ternary solvent method for MHP NCs was achieved by using naphthene, n-tridecane, and n-nonane as the solvents which do not deteriorate the properties of MHPs.[172] The introduction of a third solvent, n-nonane, which has a relatively low boiling point (151 °C), prevented the aggregation of MHP NCs compared to naphthene:n-tridecane dual solvents and accelerated solvent evaporation, resulting in uniform patterns with fewer surface defects in the final patterns (Figure 13c).[172]

The precise control of the ink viscosity is important as the coffee-ring phenomenon can be alleviated with enhanced viscosity along with a weakened capillary flow. For instance, upon the mixing of cyclohexylbenzene and nonane at a 8:2 ratio, the optimal viscosity (≈1.96 cP) of the MHP ink and the increased contact angle of the droplet resulted in a weakened capillary flow, leading to coffee-ring-free patterns of 306 PPI.[169] By using this strategy, pixelated QLEDs (pixel size of several millimeters) were also demonstrated, however, the maximum luminance and EQE of the pixelated QLEDs were somewhat limited (8533 cd m^{-2} and 0.55%, respectively). In addition, polymer mixing is one of the most promising strategies to control the viscosity of ink, by controlling the outward capillary flow. Recently, in situ inkjet printing was reported using long-chain poly(vinyl pyrrolidine) (PVP) to secure high-resolution during inkjet printing through viscosity control (Figure 13d).[173] Along with the suppressed coffee-ring effect, the C=O groups in PVP ensures a uniform size distribution of $CsPbBr_3$ upon in situ crystallization, which subsequently occurs after printing of PVP with $CsPbBr_3$ precursors.[173] Polymer-mixed ink with high viscosity can also assist the uniformity of the pattern in EHD printing. For example, the incorporation of PVP as an additive resulted in a viscosity enhancement (from 10.39 cP to 610.33 cP), and consequently, homogeneous coffee-ring-free patterns were achieved as a non-uniform Marangoni flow inside the droplet was significantly weakened.[167] The use of PVP also prevented the agglomeration of $CsPbBr_3$.

Recently, the importance of the post-annealing of inkjet-printed patterns has been highlighted.[12] Post-thermal annealing of inkjet-printed $CsPbBr_3$ layers in a vacuum oven can affect the evaporation rate of solvent, improving uniformity. Compared to the annealing done in ambient atmosphere (with a hot plate or a convection oven), the vacuum annealing resulted in faster evaporation of solvents at uniform rate, which resulted in reduced aggregation of printed $CsPbBr_3$.[12] However, despite the improved uniformity, the resulting patterns showed relatively low PLQY (20%) after the post-annealing process compared to the pristine $CsPbBr_3$ NC ink (PLQY = 87%).

4.3. Template-Assisted Printing and Direct Laser Writing

Various template-assisted patterning methods, such as nanoimprinting and transfer printing, have been applied to the patterning of light-emitting materials. Once a template (mold) is defined, a large number of samples can be repeatedly fabricated. The template-based patterning with simple processing step is free of using solvents and advantageous in terms of cost, as well as its reliable precision over a large area. However, the line-edge roughness induced by physical pattern damage during the template lift-off step is considered as one of the main limitations.

The most basic form of template-based printing is contact printing.[174] Upon the deposition of QDs on a bare substrate, the QD patterns are subsequently transferred to the target substrate with stamps. Typically, elastomers such as polydimethylsiloxane (PDMS) are used to fabricate the transferring stamps. Since the surface properties of the stamp and the QDs are critical to achieve high-yield transfer process, interlayers can be added to adjust the wettability between the interface of the QDs and the substrates. The adhesion between the emissive layers and the substrates can be adjusted by applying a self-assembled monolayer (SAM), such as octadecyltricholorisilane (ODTS), to reduce the surface energy of the substrates.[175,176]

To improve line-edge roughness, additional step using intaglio-trenched substrate was utilized.[177] By ensuring light contact of the QD layer to the intaglio trench with subsequent slow detachment, the patterns transferred to the target substrate resulted in remarkably improved line-edge roughness levels and an ≈6 µm pixel size (**Figure 14**a,b). Although high throughput can be achieved with a simple patterning process, the limited reproducibility upon repeated printing remains as a challenge. As the printing cycle is repeated, the gradual degradation of the stamp topography restricts reproducibility in defect-free pixel arrays.[178]

Recently, the immersion transfer patterning technique minimized the degradation of QD layers during the transfer process.[178] The patterning process requires proper selection of the solvent, which should be compatible with both the elastomer template and QDs. By immersing the QD layer in acetone to remove the PMMA template, a thermodynamically driven transfer process was enabled (Figure 14c).[178] The immersion transfer printing method demonstrated very high resolution of 368 PPD (considering 2-in. viewing distance, pixel size ≈ 3 µm), although the uniformity of patterns should be further improved. The authors also demonstrated patterned QLEDs with sub-pixel size of several millimeters, showing the potential of the immersion transfer printing method.

Direct laser writing has gained attention as a simple high-resolution (sub-micrometer sized pattern) patterning method for MHPs. The direct laser writing can induce the formation of MHPs even inside transparent media such as polymer[179] or glasses.[180] For instance, laser exposure to the targeted local area in situ crystallizes MHPs by providing sufficient energy for crystallization, creating MHP patterns in PMMA (Figure 14d).[179] The $CsPbI_3$ patterns with high PLQY was demonstrated using 405-nm ns laser, with minimum line-width of 0.9 µm.

4.4. Direct Optical Patterning

Direct optical patterning proceeds via a photochemical reaction of a photoactive moiety (mostly, surface ligands or additives) in the emissive ink. The photochemical reaction results in a solubility change of QDs or MHP NCs, allowing the formation of patterns. Because the photolithography steps regarding polymeric PR (such as PR deposition, baking, and lift-off) are not included in direct optical patterning, the entire patterning

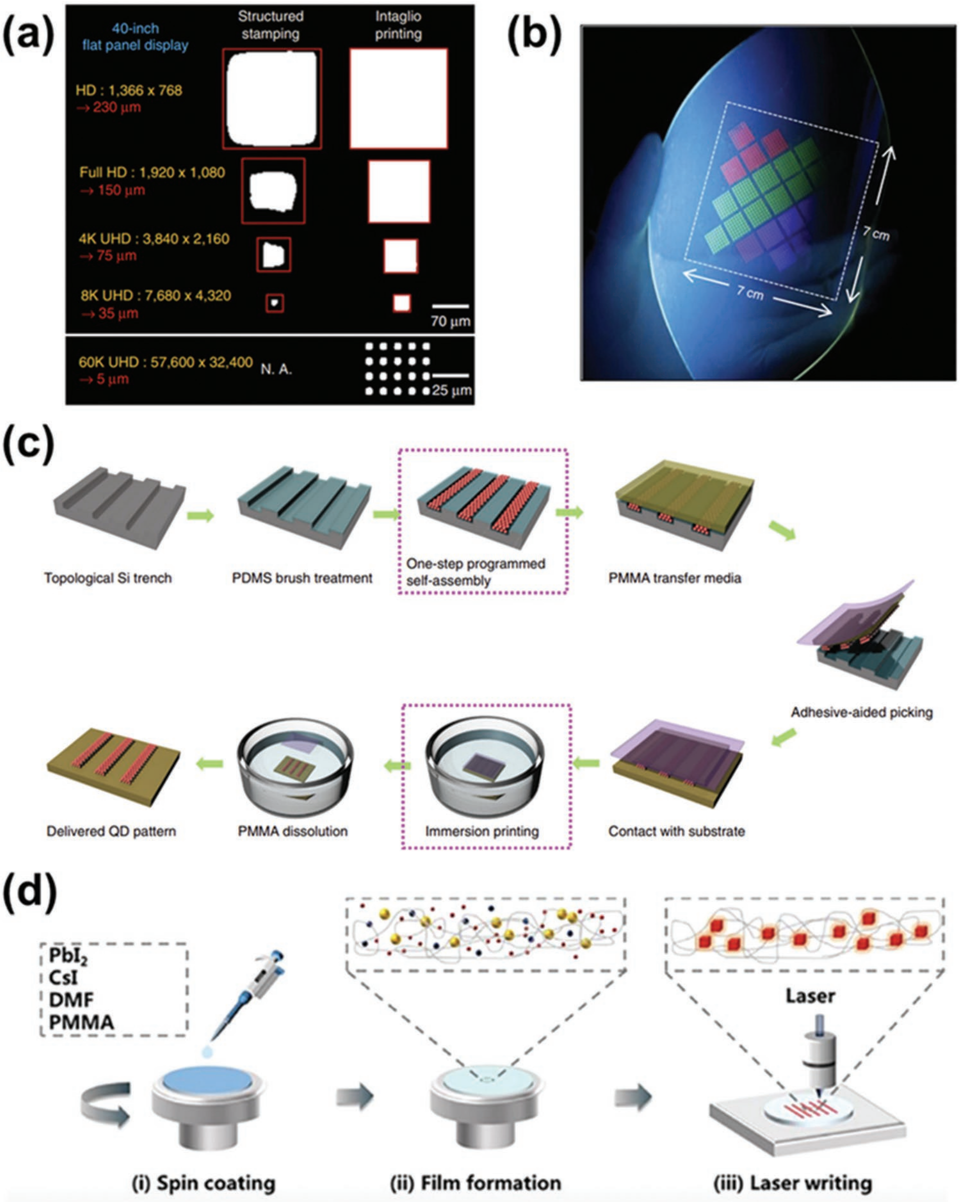

Figure 14. a) Pattern size scaling using a conventional stamp and intaglio transfer printing process. b) PL image of a large-area QD dot array created via intaglio transfer printing. c) Schematic procedure of the immersive transfer printing process. d) Schematic procedure of direct laser printing. (a, b) Reproduced with permission.[177] Copyright 2015, Springer Nature. (c) Reproduced with permission.[178] Copyright 2020, Springer Nature. (d) Reproduced with permission.[179] Copyright 2021, American Chemical Society.

procedure is relatively simple compared to traditional photolithography. The resolution limit of direct optical patterning is basically the same with photolithography, where the resolution is limited by light source and optics rather than a material issue.

As a pioneer work, direct optical lithography of functional inorganic nanomaterials (DOLFIN) method was reported by Yuanyuan and coworkers.[158] DOLFIN utilizes photopatternable NC inks, in which the NCs are functionalized with photosensitive surface ligands (or formulated with photosensitive additives), and enables the high-resolution patterning of various inorganic colloidal NCs upon UV irradiation (wavelengths of 254, 365, and 405 nm).[158,181] However, with regard to light-emitting NCs, the ligand-exchange process, which is essential for the formulation of photopatternable inks, can create more surface defects and thereby cause severe luminescence quenching.[182] To solve this problem, an advanced DOLFIN method that uses a minimal amount of photoacid generator (PAG) additives was suggested (**Figure 15**a).[157] By photochemically released acid from a traizine-based PAG (≈1–3 wt%), in situ ligand-exchange process was conducted on the surface of QDs, altering the solubility of UV-exposed area and thereby yielding high-resolution QD EL patterns (feature size down to ≈1.5 μm). Since most of the initial ligands were preserved after

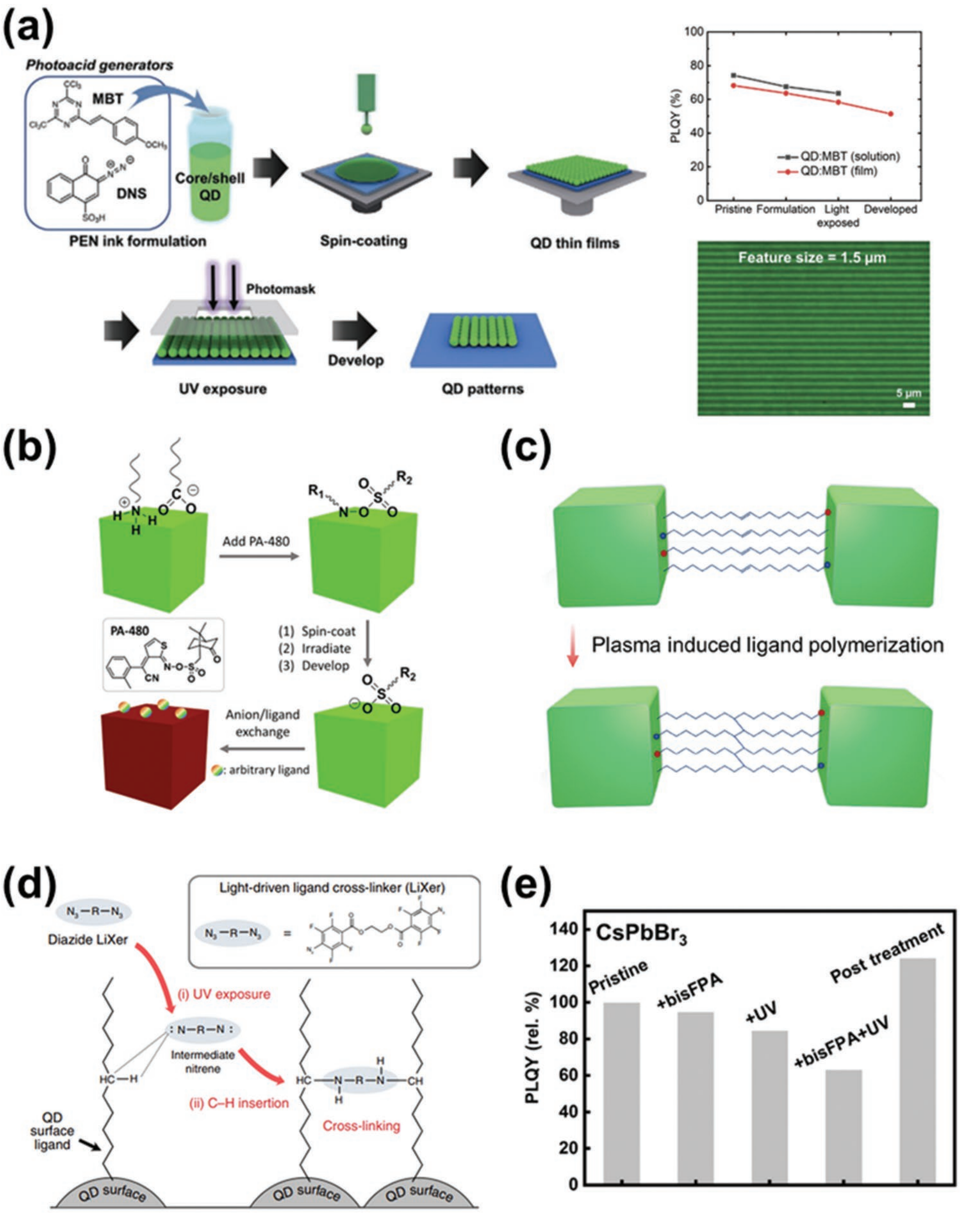

Figure 15. a) Schematic procedure of direct optical lithography with a photoacid generator, and the resulting patterns with minimized degradation. b) Schematic procedure of direct optical lithography with the photocleavage mechanism. c) Schematic procedure of direct optical lithography with high-energy optical sources. d) Schematic procedure of direct optical lithography with the azide group-based ligand bridging strategy. e) Effect of a post-treatment process on the PLQY of patterned $CsPbBr_3$. (a) Reproduced with permission.[157] Copyright 2020, Wiley-VCH GmbH. (b) Reproduced with permission.[183] Copyright 2021, American Chemical Society. (c) Reproduced with permission.[185] Copyright 2019, American Chemical Society. (d) Reproduced with permission.[191] Copyright 2020, Springer Nature. (e) Reproduced with permission.[190] Copyright 2022, American Association for the Advancement of Science.

the patterning process, the PLQY drop of QD films was able to be reduced to ≈25% of initial PLQY.[157] As another extension of DOLFIN, an oxime sulfonate ester ($R_1{-}C{=}N{-}OSOO{-}R_2$) ligands was used for the patterning of $CsPbX_3$ NCs on which the N—O bond was cleaved upon UV irradiation, leaving SO_3^- groups (Figure 15b).[183] Although an ≈1 μm line width was achieved, the PLQY of the $CsPbX_3$ NC pattern was significantly reduced after going through the patterning process; the PLQY drop was able to be restored with post-treatment, which is discussed later in this section.

Another type of direct optical patterning is to induce crosslinking between surface ligands by 1) a direct connection between ligands and 2) bridge formation between ligands with the use of a bridging additive molecule. The simplest ligand-crosslinking reaction is based on the most conventional ligands used in colloidal NCs, oleate and oleyl amine. As the double bonds included in conventional ligands were broken by high-energy optical sources (e.g., X-ray,[184] Ar plasma,[185] DUV/EUV[186,187]), crosslinking between the ligands of adjacent NCs was formed (Figure 15c). For instance, $CsPbX_3$ patterns were obtained by using a low flux X-ray (10^{11} photons mm^{-2} s^{-1}), inducing the C=C crosslinking of oleate ligands on the neighboring NCs.[184] However, the main drawback of this crosslinking strategy utilizing high-energy sources is that the optical properties of QD (or MHP) patterns can be easily degraded by the high-energy exposure. As an alternative method, UV-crosslinkable polymeric ligands that include a cinnamoyl functional group was introduced via a ligand-exchange process of $CsPbBr_3$ NCs.[188] As the cinnamoyl groups of the ligands underwent cycloaddition reactions upon UV exposure (dose: 0.15 mW cm^{-2} at 365 nm), RGB sub-pixels with the feature size of 40 μm × 10 μm (corresponding to ≈465 PPI) were demonstrated. Recently, another direct crosslinking strategy using a benzophenone moiety as a crosslink-able group has been reported.[160] Since the required dose of relatively low (35 mJ cm^{-2} at 365 nm) and only <10 mol% of native ligands (oleate) was exchanged with the crosslink-able ligands, the patterned QD films retained >95% of absorbance but PLQY dropped by ≈25% during the patterning process. The photo-crosslinked QLED showed a comparable current density and EQE (≈20%) with the pristine QLED.[160]

Also, the use of bridging molecules, which have various functional groups such as azide ($R{-}N{=}N^{+}{=}N^{-}$),[189–191] azirine ($R_1{-}CH_2N_2{-}R_2$),[192] is another effective strategy to pattern QDs or MHP NCs while minimizing the PLQY drop during the patterning process. Recently, fluorinated bisazide molecules have been investigated as a promising crosslinker;[190,191] the azide group forms a highly reactive nitrene intermediate under deep UV exposure (dose: 0.4 mW cm^{-2}), leading to subsequent C—H insertion reaction and crosslinking between oleate ligands (Figure 15d).[191] The effect of crosslinking on the optical and electrical properties of the QD films was nearly negligible, as demonstrated by the crosslinked QLED showing comparable device characteristics with the control device. A multi-color pixel array with 1400 PPI was also demonstrated.[191] In another study, the same bisazide crosslinker was used for the patterning of $CsPbBr_3$ NCs, retaining 60% of the initial PLQY after patterning process.[190] Recently, the influence of photochemical reactions, which highly depend on the chemical structure of crosslinker molecules, on the patterning capability was in-depth investigated by comparing various azide-based and azirine-based crosslinkers.[192] Azirine-based crosslinkers, which use carbene radical-involved photo-triggered reactions, showed significantly higher retention rates of the PLQYs (≈90% of initial PLQY) and fully preserved EL characteristics compared to azide-based crosslinkers.[192]

As mentioned above, PL quenching after such a patterning process is one of the most critical challenges for the direct optical patterning of colloidal QDs and MHP NCs. The primary origin is that the photosensitive ligands or additives can induce a higher density of un-passivated surface trap sites during such photo-induced reactions. To overcome this challenge, a post-treatment was introduced to avoid such PLQY drop.[183,190] By applying a defect-passivating solution composed of free ligands and an orthogonal solvent to the patterned films, the surface traps can be passivated. For instance, a post-treatment using a solution containing $PbBr_2$, octanoic acid, and butylamine successfully restored the PLQY of patterned $CsPbX_3$ films (from 5% to 79%).[183] Similarly, after going through the patterning process based on azide-based crosslinking, a post-treatment process using $PbBr_2$, oleyl amine and oleic acid substantially increased the PLQY of the patterned $CsPbBr_3$ films to the level (≈120%, relatively) even higher than that of pristine films (Figure 15e).[190] Also, the patterned $CsPbBr_3$ PeLED showed a higher EQE (6.8%) compared to the un-patterned control device (≈6%).

5. Applications of Nanoscale Emitters

5.1. Down-Conversion PL with QD and MHP Emitters

Recently, colloidal QDs have been utilized as down-conversion materials (in QDEF or QDCF) located on a blue backlight unit in commercial displays. Displays equipped with such QD (or MHP) color-conversion layers can show significantly improved color gamut, achieving ≧85% of the Rec.2020 standard, whereas conventional inorganic phosphors cover only ≧60% of the Rec.2020.[193]

The inevitable optical loss can occur as light passes through the diffractive optical system of AR/VR devices.[194] In case of a slim optical system for miniaturized devices, only 25% of initial luminance is maintained due to the optical loss.[195] Therefore, high luminance over 100 000 nits (cd m^{-2}) is necessary to compensate such loss and provide sufficient luminance, especially for AR devices. In addition, the absorption coefficient of color conversion materials should be further increased for achieving higher color conversion efficiency, as well as decreasing the thickness of the color conversion layers. Also, the thickness and uniformity of the color conversion layer should be optimized as they can greatly affect the conversion efficiency.[196] In this section, we review state-of-the-art studies that used colloidal QDs or MHP NCs as a color conversion layer, focusing on device structure and color conversion efficiency.

5.1.1. Down-Conversion PL with QDs

As previously mentioned, colloidal QDs are highly suitable as a color conversion layer of displays since the QD color conversion layers can provide enhanced color gamut (exceeding that of conventional inorganic phosphors), color tunability, and high stability.[197]

Typical display panel structures incorporating QDEF and QDCF are shown in **Figure 16**a,b. Current applications of QDs to liquid crystal displays (LCDs) mainly utilize a QDEF layer on top of a blue backlight unit (Figure 16a). The common QDEF comprises green- and red-emitting QDs embedded in a polymer matrix and the QD:polymer films are encapsulated with transparent films.[198] The commercial QDEF-based high-resolution televisions demonstrated by Samsung employed an InP-based core/shell QDs on top of blue GaN LEDs.[199] Nanosys reported 10 μm-thick QDEFs with InP-based core/shell QDs representing photon conversion efficiency of 38%.[200]

However, the Förster resonance energy transfer (FRET) phenomenon among adjacent red, green QDs can severely damage the light conversion efficiency of QDEFs.[201] To minimize the FRET phenomenon, the interaction among QDs

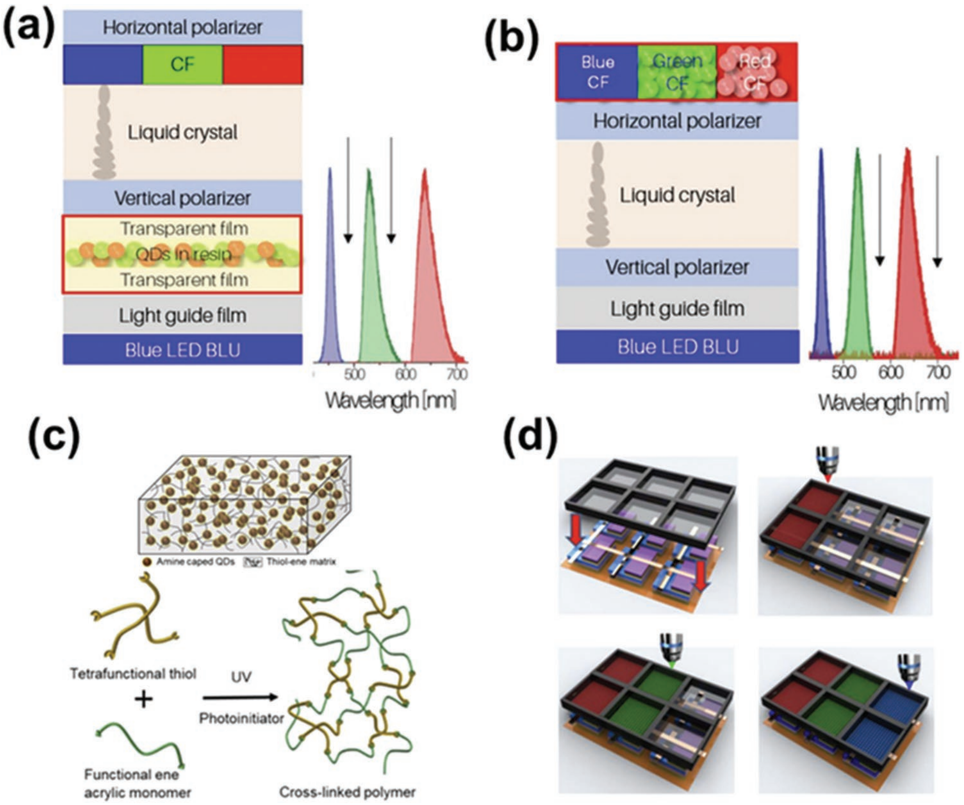

Figure 16. a) Schematic of the QDEF structure. b) Schematic of the QDCF structure. c) Schematic of the crosslinking approach used for a uniform distribution of QDs. d) Schematic of the light-blocking wall structure to prevent the optical crosstalk phenomena. (a, b) Reproduced with permission.[198] Copyright 2020, Springer Nature. (c) Reproduced with permission.[204] Copyright 2019, Optica Publishing Group. (d) Reproduced with permission.[205] Copyright 2017, Optica Publishing Group.

should be reduced; in this respect, a low concentration of QDs in QD/polymer composites may be desirable. However, excessively reduced amount of QDs can also lead to a low color conversion efficiency and emergence of unfiltered blue light; therefore, considering this trade-off relationship, finding an optimal concentration of QDs is crucial.[198] To further increase the blue light absorption of QDEFs, the incorporation of light scattering media such as TiO_2, SiO_2, and 2D nanoplatelets has also been investigated.[14]

The QDCF is the next-generation QD display architecture in that the QDCF can provide high color conversion efficiency, high color accuracy as well as a large viewing angle (Figure 16b).[202] In QDCF-type displays, red and green colors are achieved by color conversion with QDs, while the blue color is directly achieved from the blue backlight unit. QDCFs should have a sufficient thickness (typically, several micrometers) for complete color conversion without transmitting blue backlight.[203] Also, for both QDEF and QD:polymer composite CFs, uniform distribution of QDs in the polymer matrix is essential to maximize color conversion efficiency. A photopolymerizable polymer (NOA86) with a thiol-ene group has been used as a host polymer showing uniform distribution of CdSe/ZnS core/shell QDs (Figure 16c).[204] The QD/photopolymer composite was patterned using projection lithography, showing color gamut corresponding to 95% of the DCI-P3 standard.

The improper patterning of QDCFs may result in the color cross-talk phenomenon: color blending of a pixel with the other colors of adjacent pixels. To overcome this, light-blocking walls between QDCF pixels should be additionally incorporated. The bank structure among the pixels should be deposited prior to the emission layer to minimize the degradation of the emissive layers. For instance, the light-blocking wall can be constructed using a PR-defined mold via the lithography technique, with the subsequent deposition of QDs (Figure 16d).[205] However, the uniform, high-resolution selective deposition of QDs on the bank structure is challenging due to the capillary force at the QD/bank interfaces.

5.1.2. Down-Conversion PL with MHPs

Compared to CdSe-based and InP-based QDs, MHPs have higher color purity levels (color gamut ratio > 140%) and higher absorption coefficient,[18] which makes MHPs suitable for color conversion applications. However, as previously mentioned in Section 3.2, the poor stability of MHPs against external factors such as polar solvents, moisture, oxygen, heat, and light requires MHPs to be well passivated and encapsulated to fulfill the stability requirement of the color conversion layer. Therefore, strategies to enhance the structural and interfacial stability levels using encapsulants are vital for practical applications of MHPs.

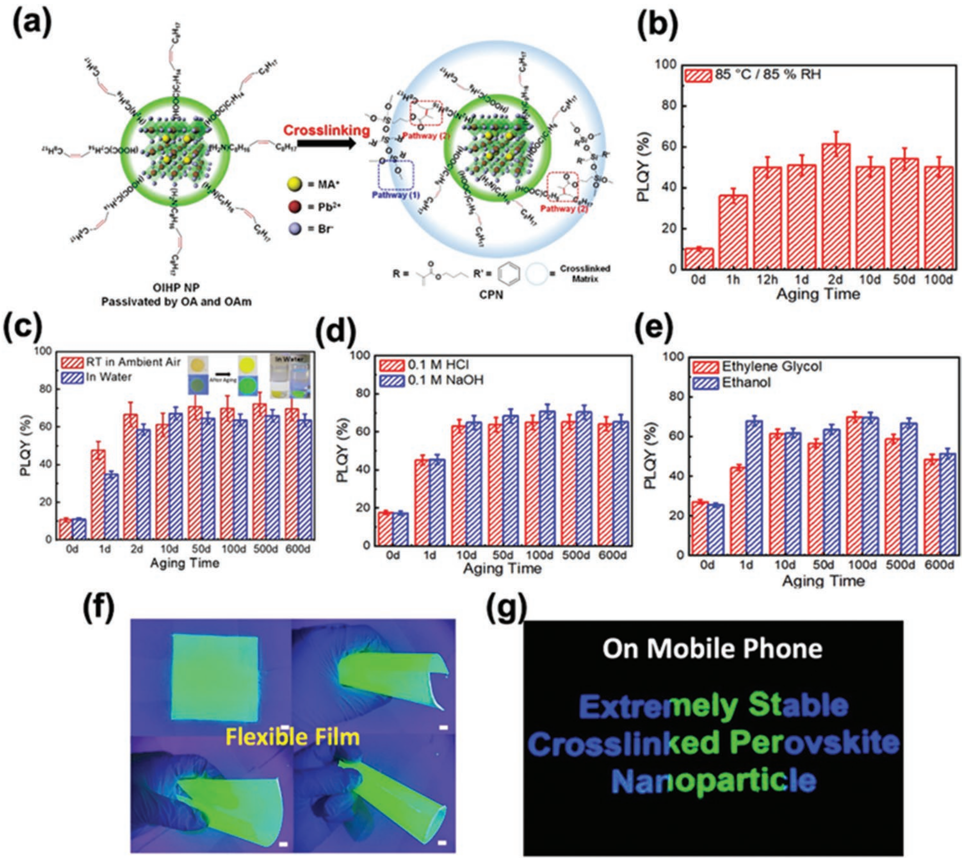

Figure 17. a) Schematic illustration of the formation of crosslinked perovskite nanoparticles (CPNs). Stability of CPN under harsh conditions. b) 85 °C/85%RH, c) under ambient air at RT and in water, d) in acid and base solutions, and e) in ethylene glycol and ethanol. f,g) Flexible large-area (size: 10 cm × 10 cm) green-emitting CPN films under bending and CPN on a mobile phone. Reproduced with permission.[218] Copyright 2020, Wiley-VCH GmbH.

Various approaches have been devised to enhance the stability of MHPs using inorganic materials[206,207] or polymer encapsulants[208–217] that can effectively encapsulate MHPs and prevent them from contact with external stimuli. However, most composites still show limited stability under harsh conditions, and MHPs tend to aggregate in the matrix. Hence, methacrylate functional groups are introduced into the matrix resin to crosslink chemically with the unsaturated oleic acid and oleyl amine ligands; this forms a dense film that can prevent the diffusion of oxygen and moisture.

Methylammonium lead bromide ($MAPbBr_3$) NCs were initially dispersed in a precursor of resin (3-methacryloxypropyl) trimethoxysilane (MPTS) and diphenylsilanediol (DPSD)) and were then heated to an elevated temperature (80 °C) to induce a chemical reaction between the methoxy group of MPTS and the hydroxyl groups of DPS. Finally, after solidification via UV curing, two free-radical cross-linking reactions occurred, forming a highly condensed SiO_2-like matrix with $MAPbBr_3$ NCs uniformly distributed inside (**Figure 17**a).[218] To evaluate the stability of the crosslinked perovskite NCs (CPNs), the PLQY was measured under various aging conditions. CPNs that are aged under 85 °C/85% RH showed increased PLQY to 60% and the value was retained after 100 days (Figure 17b). CPN shows excellent stability in air, water, acid, base solutions, in ethylene glycol, and in ethanol for >1.5 years (600 days) (Figure 17c–e); this is one of the most stable reported MHP composites. The CPNs were successfully applied to large-area flexible green-emitting films (Figure 17f) and as a blue-to-green color conversion layer on a mobile phone (Figure 17g).

However, with the rapid development of wearable electronics with free form factors, stretchable displays have become the most important platform for the visualization of wearable sensor signals. Current stretchable light-emitting devices require an excellent stretchable encapsulation layer, representing a serious bottleneck in the development of stretchable displays. The solution is to develop intrinsically stretchable light-emitting devices that are stable in air without encapsulation and to use an air-stable stretchable color conversion layer (SCCL) to provide a new route to solve the stretchable encapsulation problem.

Among all thermoplastic elastomers, styrene-ethylene-butylene-styrene (SEBS) was chosen as the matrix for the $MAPbBr_3$ NCs dispersion, as SEBS has higher miscibility with oleic acid.[219] To form a free-standing SCCL, NCs were synthesized and dispersed in SEBS. The SCCL can be stretched to 120% without mechanical degradation (**Figure 18**a). During the water stability test, the PL intensity of the SCCL increased to 225% after 70 days; this was found to be induced by either

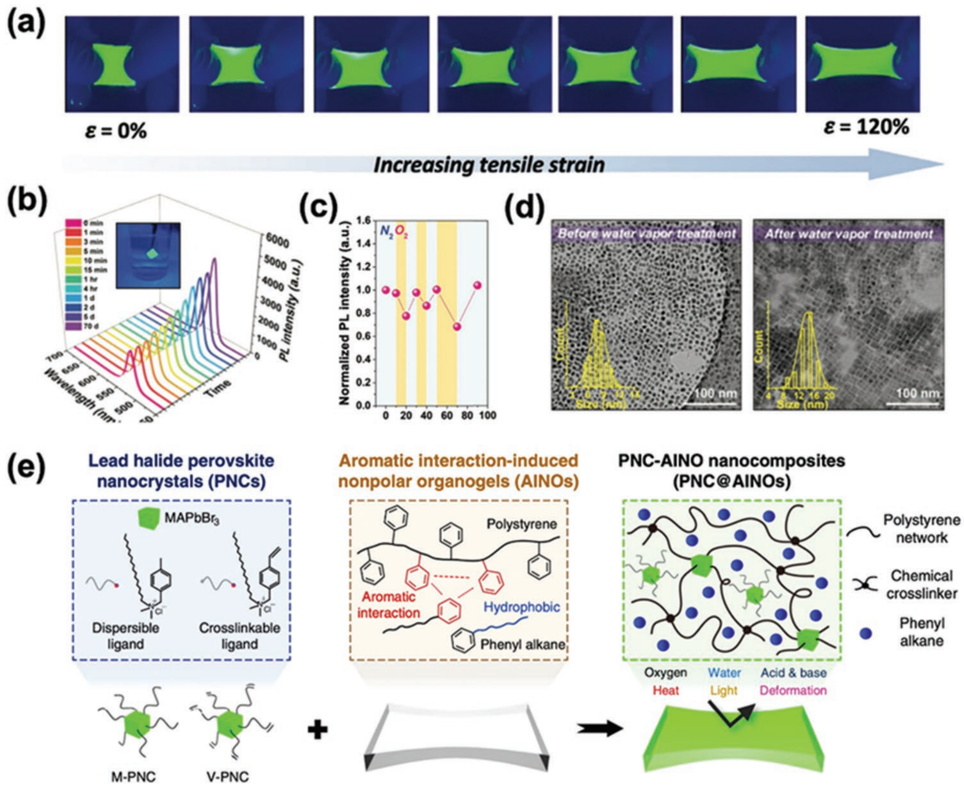

Figure 18. a) Photographs of a stretchable color conversion layer (SCCL) with an increase in the tensile strain to 120%. b) Revolution of the PL spectra of SCCL after immersion in water up to 70 days. c) Evolution of the PL peak intensity of the PeNC solution under an alternating flow of O_2 and N_2 at 100 sccm min^{-1}. d) High-resolution transmission electron microscopy (HR-TEM) images of PeNCs before and after a water vapor treatment. e) Schematic illustration of a synergistic combination of lead halide perovskites ($MAPbBr_3$) and aromatic interaction-induced nonpolar organogels (AINOs). (a–d) Reproduced with permission.[219] Copyright 2020, Wiley-VCH GmbH. (e) Reproduced with permission.[220] Copyright 2020, Springer Nature.

oxygen or moisture (Figure 18b). However, the oxygen stability test clearly showed that the oxygen atoms that quench the PL intensity were only physically adsorbed into the NCs without chemical reactions (Figure 18c); this was found to be induced by the structural change accompanied by the water-assisted passivation of the NCs (Figure 18d). An air-stable intrinsically stretchable display that is composed of an SCCL and intrinsically stretchable blue EL components is successfully achieved and can undergo 180% of strain.

As an alternative to thermoplastic elastomers, stretchable and transparent aromatic interaction-induced nonpolar organogels (AINOs) can be used for $MAPbBr_3$ NC dispersion (Figure 18e).[220] The NCs were chemically anchored to the stretchable AINO matrix and showed bright luminescence with a PLQY of 99.8%; this may also enable a step forward toward the next generation of stretchable optoelectronic devices.

5.2. EL of QDs and MHP Emitters

Future AR/VR displays should ultimately have lighter, smaller device hardware with superior performance capabilities (e.g., brightness and color gamut) than those of current AR/VR displays. To fulfil this requirement, EL-based displays are promising since the pixels self-illuminate without backlight unit with much higher power efficiency than PL-based displays.[221] Because backlight conversion is not required, a very high contrast ratio and bendable/foldable form factor can be achieved.[177,222] The absence of backlight unit can also contribute to the expanded viewing angle. In addition, the use of QDs and MHPs as an emission layer can significantly improve the color gamut of EL-based displays. However, the EL-based displays are still in the early stages of development.

The general structure of EL-based displays comprises anode, hole injection/transport layer, emission layer (RGB), electron injection/transport layer, and cathode (**Figure 19**a). Every RGB pixels should demonstrate high EL efficiency and stability to realize commercial EL-based displays. Thus far, the highest EQE values reported for InP-based QLEDs are 22.2%, 16.3%, and 2.6% for red, green, and blue, respectively.[24,77,223] In case of MHPs, the best EQE values reached 24.4% for red, 23.4% for green, and 12.8% for blue PeLEDs.[23,25,224] In addition, the device lifetime should reach at least several tens of thousands of hours at 1000 cd m^{-2} for practical applications.[225] Up to date, the maximum device lifetime of QLEDs recorded T_{95} value of ≈580 000 h at 100 cd m^{-2}, while the maximum value of PeLED is limited under several hundreds (T_{50} = 317 h at 30 mA cm^{-2}).[226,227] Further studies should make improvement on current challenges of EL-based displays, which includes the followings: 1) low device lifetime, 2) low EQE of blue LEDs, 3) toxic elements, 4) limited stretchability.

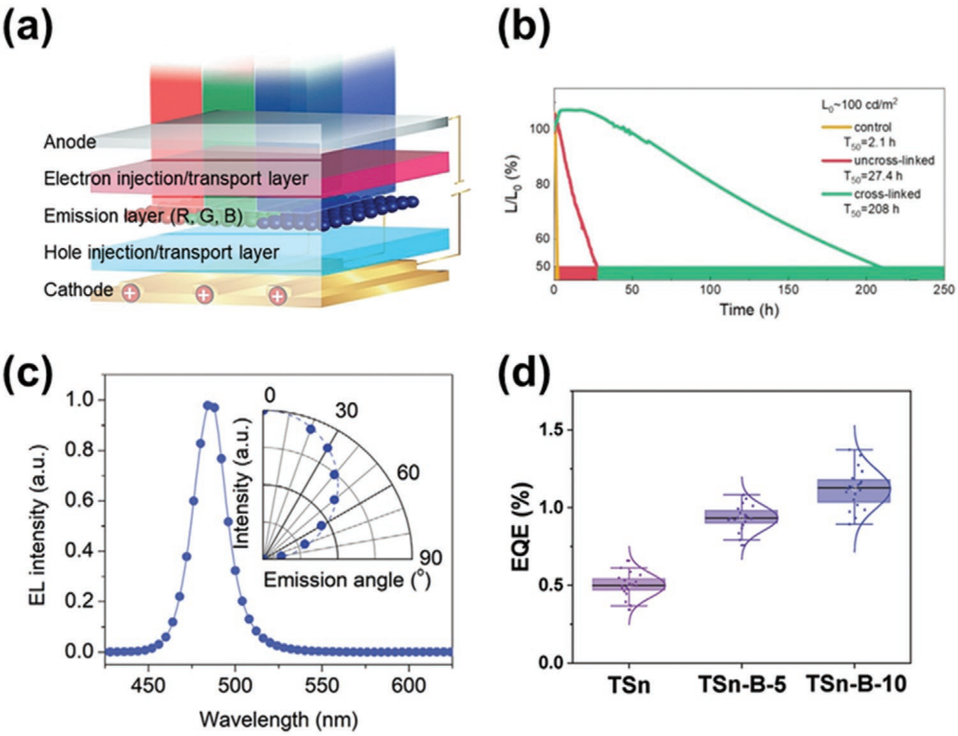

Figure 19. a) Schematic of the EL-based device structure. b) Lifetimes of LEDs based on control, uncross-linked, and cross-linked MHP layers. c) EL emission spectra of blue perovskite LEDs. d) Device efficiency Sn-based MHPs. (a) Reproduced with permission.[221] Copyright 2018, Wiley-VCH GmbH. (b) Reproduced with permission.[228] Copyright 2021, Wiley-VCH GmbH. (c) Reproduced with permission.[224] Copyright 2021, Wiley-VCH GmbH. (d) Reproduced with permission.[231] Copyright 2021, Wiley-VCH GmbH.

The low operational lifetime is especially problematic in PeLEDs. The degradation of MHP emission layer, originating from intrinsic instability of MHPs, can be accelerated under device operating condition (e.g., electric field-induced ion migration), which consequently affects the instability of PeLEDs.[8] To improve the stability of MHP layers, complete passivation of surface defects such as halide vacancies is necessary. The in situ addition of inorganic NaI ligand could effectively passivate the trap sites, resulting in decreased halide vacancies and subsequent suppression of phase segregation.[25] Although the operational lifetime of NaI-passivated PeLED increased by six times compared to the pristine device, it still resulted in limited T_{50} (≈20 h). In addition, the acrylamide ligand crosslinking-induced passivation of halide vacancies at grain boundaries was reported, reaching an operational lifetime of 208 h due to suppressed ion migration (Figure 19b).[228] Additional interlayer for charge balance can further contribute to the improvement in device lifetime. For instance, the introduction of ≈5 nm thick 1,3,5-tris(bromomethyl)-2,4,6-triethylbenzene interlayer on top of $FA_{0.9}GA_{0.1}PbBr_3$ layer demonstrated more than five times enhanced T_{50} value (132 min) compared to the control device (25 min).[23]

Despite the significant improvement in EL efficiency of red and green LEDs, the efficiencies of blue QLEDs and PeLEDs are falling behind them. In case of InP-based blue QLEDs, the low EL efficiency is largely attributed to the defects at the core/shell interfaces. The interfacial defects mainly arise from the lattice mismatch between InP core and ZnS shell. The highest EQE of blue InP-based QLEDs was achieved through surface defect passivation by $ZnBr_2$ and ligand exchange to 1-octylthiol, however, the value is still limited under 5%.[223] Another candidate for Cd-free blue emission is ZnSeTe. Recently, 18.6% high efficiency have been realized with ZnSeTe-based QLED, which exceeds the InP-based counterparts.[229] For blue PeLEDs, the maximum EQE of 12.8% was reported.[224] However, the emission peak of the PeLED was located at 486 nm (sky-blue), which is not suitable as a Rec.2020 emitter (Figure 19c). The mixed-halide composition engineering (e.g., $CsPbCl_{0.5}Br_{0.5}$) is frequently used to realize pure-blue emission (467 nm), but often suffer from halide segregation problem under device operation.[230]

The development of lead-free PeLEDs is still in its infancy in terms of both the EQE and the stability, which is mostly due to the insufficient PLQY value and low material stability. Currently, world-record EQE values of red, green, and blue lead-free PeLEDs do not exceed 10%. Hence, further improvements in both EQE and device lifetime are imperative.[139,231–234] For instance, Sn-halide PeLEDs resulted in 1.37% EQE and T_{50} under 5 min, even though oxidation of Sn^{2+} was suppressed by stabilization of Sn-I framework using biuret additive (Figure 19d).[231]

Although current AR/VR displays exhibit a head-mounted device structure, the progress in EL-based displays will eventually lead to the realization of wearable displays. Recent progress in mechanics and stretchable materials makes it possible to develop wearable/stretchable electronics.[235] Stretchable displays have become one of the most important output media for the direct visualization of signals from various sensors attached to human skin. This requires the stretchable display to endure various mechanical deformations, such as bending, twisting, and stretching.[236] However, stretchability is even more challenging as it requires the entire device structure to endure large tensile strain without inducing any mechanical failure within the device. As a replacement for rigid glass or silicon substrates, stretchable displays are fabricated on thin polymer substrates that can be either structurally or intrinsically stretchable.[237]

To achieve a geometrically stretchable structure, the device should be either fabricated using an island bridge[238] or with out-of-plane buckling structures[239] depending on the specific application. The former consists of electroluminescence (EL) devices on rigid islands with wave-like stretchable interconnects that endure most of the strain applied to the device; this approach has not been achieved using MHPs, as it requires the solution-processed light-emitting layer to be deposited onto a specific area for the following lift-off process. Hence, the buckling structure becomes a more general approach to making the device stretchable. Unlike the in-plane island-bridge structure with EL units and interconnects located on the same plane, the ultrathin EL unit forms an out-of-plane buckling structure after releasing the strain of the pre-strained substrate. Given the fact that bending strain is proportional to the thickness of the substrate,[240] controlling the thickness of the EL units together with the substrate to the µm scale is vital to alleviate the effect of the tensile strain. In practice, the ultra-thin substrate thickness should be less than 2 µm to form wrinkles with a small wavelength.[239]

The geometrically stretchable PeLED was first achieved using the an ultrathin polyimide (PI) substrate of 1–2 µm with silver nanowire (AgNW) embedded into it.[241] The electrode was then transferred onto a pre-stretched elastomer adhesive (VHB 4905) with 50% of strain. To enhance the hole injection and reduce the hole injection barrier, a molecularly blended hole transport layer was used. The PeLED showed a turn-on voltage of 3.3 V and maximum current efficiency of 9.2 cd A^{-1}. The strategy for creating the buckling structure on the PeLED ensures the maximum tensile strain of 50%, showing uniform light emission throughout the stretching cycles without inducing mechanical failure. The geometrically stretchable PeLED showed only a 25% loss in the EL intensity after 1000 cycles of stretching at 50% of strain.[241]

However, compared to state-of-the-art PeLEDs with maximum current efficiency exceeding 100 cd A^{-1}, a more precise design of the interfacial energy level alignment is necessary. Specifically, due to the low work function of AgNW, it is challenging to achieve efficient hole injection. Conducting polymer electrodes with a high work function could be an effective approach to address this problem.[23]

Unlike using the geometrically stretchable devices that use specific structures to mitigate the strain, intrinsically stretchable devices require all layers in light-emitting devices to be stretchable. Hence, to enhance the stretchability, MHPs are mixed with materials that have a lower modulus. The $MAPbBr_3$ precursor was blended with polyethylene oxide (PEO), which functions as the matrix to achieve stretchability.[242] It was found that in situ $MAPbBr_3$ NCs embedding in the PEO matrix without pinholes were formed during the solution process, making the MHP emission layer stretchable. The stretchable PeLED was fabricated by the deposition of liquid-metal eutectic gallium indium (EGaIn) as the stretchable cathode. The intrinsically stretchable PeLED showed a low turn-on voltage of 2.4 V and maximum luminance of 15 960 cd m^{-2}, which is the highest reported value achieved in stretchable light-emitting devices.[242]

Despite the excellent EL properties of PeLEDs, including their high EQE and narrow FWHM compared with organic emitters, the development of stretchable PeLEDs is still in a very early stage. MHPs could be a promising candidate for stretchable applications if the mechanical robustness can be enhanced without sacrificing the EL properties in the future.

6. Summary and Perspectives

We have discussed the current recent progress of AR/VR technologies and emerging emitter technologies (colloidal QDs and MHPs) for use in AR/VR display devices. The structural/optical properties and synthesis methods of the QDs and MHPs were briefly reviewed considering display applications. Also, various synthetic approaches to achieve high PLQYs, emission linewidths, and stability of the light emitters were discussed. Currently, state-of-the-art InP-based core/shell QDs and $CsPbX_3$ NCs show near-unity PLQYs in green and red colors. In terms of the emission linewidth, $CsPbX_3$ NCs exhibit greater potential than do InP QDs (e.g., FWHM in green: <20 nm for $CsPbBr_3$ NCs and ≈35 nm for InP-based core/shell QDs). Particularly, the stronger optical absorption of MHPs compared to InP QDs provides an opportunity to increase the color conversion efficiency with a reduced thickness of the color conversion layer.

However, several technical challenges in both material and process aspects must be overcome to realize QD- or MHP-based AR/VR NEDs. With regard to materials, the major challenges include 1) the realization of efficient red, green, and blue emitters that satisfy Rec.2020; 2) low thermal, photo and color stability; 3) low stability and device efficiency blue QD and MHP emitters, and 4) mitigating the toxicity of lead halide perovskites.

The emission wavelengths of the high-PLQY QD and MHP emitters should be adjusted to satisfy the standard wavelength of Rec.2020 (red: 638 nm, green: 532 nm, blue: 467 nm). InP-based QDs can cover the 638-red and 532-green colors by precise size control while maintaining high PLQYs. Because the precise synthesis of InP QDs becomes more difficult as the size decreases, the realization of blue InP-based QDs with high PLQYs and stability is still challenging. For colloidal MHP NCs, wavelength tuning is typically performed through compositional engineering, as the sizes of the NCs usually lie in the regime beyond the quantum size effect (i.e., NC size > exciton Bohr diameter). For green-emitting MHP NCs, the emission peak wavelengths of $CsPbBr_3$ and $FAPbBr_3$ NCs are ≈520 and 530–540 nm, respectively; therefore, wavelength modification through A-site cation engineering is required to satisfy Rec.2020. The synthesis of blue-emitting MHP NCs with high PLQYs and stability is even more challenging than the synthesis of blue InP QDs. The use of Cl-Br mixed-halide perovskites is often used to achieve the 467-blue color. Alternatively, the 467-blue color can also be achieved by using pure-Br MHPs with quantum size effect or a quasi-2D crystal structure.[243,244]

However, the photo/bias-induced halide segregation originating from the intrinsically weakly bonded ionic lattice of MHPs limits the color stability. Also, the external stresses result in ion migration in the MHP lattice and contribute further to structural degradation, leading to low material stability. Therefore, to realize highly efficient and stable red, green, and blue MHP emitters, future studies should focus on developing compositional engineering and defect passivation strategies to prevent halide segregation and ion migration and thereby completely overcome the stability issues at the standard wavelengths of Rec.2020.

Also, in AR NEDs, the luminance should be on the order of 10^5 cd m^{-2} (desirably, $\approx 10^6$ cd m^{-2}) considering outdoor use and the large optical loss in the optical combiners. Such high brightness can induce severe photo-induced degradation of QD (or MHP) layers (in both down-conversion-PL and EL applications); in this respect, developing a high-stability QD or MHP emitter (or layer) that does not easily deteriorate over time at ultra-high luminance is the most important prerequisite for the commercialization of QD- or MHP-based AR NEDs.

Despite great efforts over the past few years, the development of lead-free MHP emitters showing comparable levels of PLQY and emission linewidth of lead halide perovskites is still an ongoing and challenging work. The high oxophilicity of alternative B-site metal cations (e.g., tin halide perovskites) and the existence of self-trapped excitons (e.g., double perovskites) are fundamental limitations that should be overcome in the future.

To exploit the QD and MHP emitters in AR/VR NEDs, patterning method should also be developed to achieve high-resolution RGB-patterned display panels (e.g., ≈10 000 PPI for AR). Among various methods, direct optical patterning shows great promise with pattern uniformity and simple process (without PR usage), while retaining the advantages of conventional photolithography such as high resolution up to ≈1 µm. We predict that future studies on direct optical patterning will be directed toward minimizing loss in optical and electrical properties of emitters and improving material stability. Meanwhile, the development of advanced inkjet printing or other printing methods that can achieve high resolution of >2000 PPI and uniform pattern profile will also be of great research interest.

The high-color-purity QD and MHP emitters have become core technologies that can provide a more realistic augmented/virtual experience beyond the existing NEDs. We envision that the next generation of AR/VR headsets to be based on QD and MHP emitters through technological breakthroughs in the near future.

Acknowledgements

S.J.P. and C.K. contributed equally to this work. This work was supported by the Wearable Platform Materials Technology Center (WMC) funded by the National Research Foundation of Korea (NRF) Grant by the Korean Government (MSIT) (NRF-2022R1A5A6000846). This work was financially supported by the National Research Foundation of Korea (NRF) grant funded by the Korea Government (MSIT) (NRF-2022M3H4A1A03085346). This research has been supported by the POSCO Science Fellowship of POSCO TJ Park Foundation. T.W.L. acknowledges the financial support from Pioneer Research Center Program through the National Research Foundation of Korea funded by the Ministry of Science, ICT & Future Planning (grant No. 2022M3C1A3081211).

Conflict of Interest

The authors declare no conflict of interest.

Keywords

colloidal quantum dots, down-conversion, extended reality, halide perovskites, near-eye displays

Received: July 1, 2022
Revised: September 21, 2022
Published online:

---

[1] K. Yin, E.-L. Hsiang, J. Zou, Y. Li, Z. Yang, Q. Yang, P.-C. Lai, C.-L. Lin, S.-T. Wu, *Light: Sci Appl* **2022**, *11*, 161.
[2] S. Liu, K. Ma, B. Yang, H. Li, X. Tao, *Adv. Funct. Mater.* **2021**, *31*, 2007254.
[3] K. Wang, L. W. Yap, S. Gong, R. Wang, S. J. Wang, W. Cheng, *Adv. Funct. Mater.* **2021**, *31*, 2008347.
[4] D. Matthews, *Nature* **2018**, *557*, 127.
[5] J. Xiong, E.-L. Hsiang, Z. He, T. Zhan, S.-T. Wu, *Light: Sci. Appl.* **2021**, *10*, 216.
[6] H. Moon, C. Lee, W. Lee, J. Kim, H. Chae, *Adv. Mater.* **2019**, *31*, 1804294.
[7] X. Dai, Y. Deng, X. Peng, Y. Jin, *Adv. Mater.* **2017**, *29*, 1607022.
[8] H. Cho, Y.-H. Kim, C. Wolf, H.-D. Lee, T.-W. Lee, *Adv. Mater.* **2018**, *30*, 1704587.
[9] Y. Shu, X. Lin, H. Qin, Z. Hu, Y. Jin, X. Peng, *Angew. Chem.* **2020**, *132*, 22496.
[10] X.-K. Liu, W. Xu, S. Bai, Y. Jin, J. Wang, R. H. Friend, F. Gao, *Nat. Mater.* **2021**, *20*, 10.
[11] M. Lu, Y. Zhang, S. Wang, J. Guo, W. W. Yu, A. L. Rogach, *Adv. Funct. Mater.* **2019**, *29*, 1902008.
[12] G. Vescio, J. L. Frieiro, A. F. Gualdrón-Reyes, S. Hernández, I. Mora-Seró, B. Garrido, A. Cirera, *Adv. Mater. Technol.* **2022**, *7*, 2101525.
[13] Y. Yin, Z. Hu, M. U. Ali, M. Duan, L. Gao, M. Liu, W. Peng, J. Geng, S. Pan, Y. Wu, J. Hou, J. Fan, D. Li, X. Zhang, H. Meng, *Adv. Mater. Technol.* **2020**, *5*, 2000251.
[14] H. Gao, Y. Xie, C. Geng, S. Xu, W. Bi, *ACS Photonics* **2020**, *7*, 3430.
[15] T. Meng, Y. Zheng, D. Zhao, H. Hu, Y. Zhu, Z. Xu, S. Ju, J. Jing, X. Chen, H. Gao, K. Yang, T. Guo, F. Li, J. Fan, L. Qian, *Nat. Photonics* **2022**, *16*, 297.
[16] J. Wang, N. Wang, Y. Jin, J. Si, Z.-K. Tan, H. Du, L. Cheng, X. Dai, S. Bai, H. He, Z. Ye, M. L. Lai, R. H. Friend, W. Huang, *Adv. Mater.* **2015**, *27*, 2311.
[17] Z. Ren, J. Yu, Z. Qin, J. Wang, J. Sun, C. C. S. Chan, S. Ding, K. Wang, R. Chen, K. S. Wong, X. Lu, W. Yin, W. C. H. Choy, *Adv. Mater.* **2021**, *33*, 2005570.
[18] H. Lee, J. Park, S. Kim, S. Lee, Y. Kim, T. Lee, *Adv. Mater. Technol.* **2020**, *5*, 2000091.
[19] J. Shamsi, A. S. Urban, M. Imran, L. De Trizio, L. Manna, *Chem. Rev.* **2019**, *119*, 3296.
[20] Z. Xiao, Z. Song, Y. Yan, *Adv. Mater.* **2019**, *31*, 1803792.
[21] J. S. Manser, J. A. Christians, P. V. Kamat, *Chem. Rev.* **2016**, *116*, 12956.
[22] H.-C. Wang, Z. Bao, H.-Y. Tsai, A.-C. Tang, R.-S. Liu, *Small* **2018**, *14*, 1702433.
[23] Y.-H. Kim, S. Kim, A. Kakekhani, J. Park, J. Park, Y.-H. Lee, H. Xu, S. Nagane, R. B. Wexler, D.-H. Kim, S. H. Jo, L. Martínez-Sarti, P. Tan, A. Sadhanala, G.-S. Park, Y.-W. Kim, B. Hu, H. J. Bolink, S. Yoo, R. H. Friend, A. M. Rappe, T.-W. Lee, *Nat. Photonics* **2021**, *15*, 148.

[24] H. Li, W. Zhang, Y. Bian, T. K. Ahn, H. Shen, B. Ji, *Nano Lett.* **2022**, *22*, 4067.

[25] Y. Wang, K. Singh, J. Li, Y. Dong, X. Wang, J. M. Pina, Y. Yu, R. Sabatini, Y. Liu, D. Ma, J. Liu, Z. Liu, Y. Gao, O. Voznyy, W. Ma, M. Fung, L. Liao, E. H. Sargent, *Adv. Mater.* **2022**, *34*, 2200854.

[26] B. C. Kress, *Optical Architectures for Augmented-, Virtual-, and Mixed-Reality Headsets*, SPIE, **2020**.

[27] HMD Geometry Database. https://risa2000.github.io/hmdgdb/ (accessed: May 2022).

[28] H. J. Jang, J. Y. Lee, G. W. Baek, J. Kwak, J.-H. Park, *J. Inf. Disp.* **2022**, *23*, 1.

[29] C. A. Curcio, K. R. Sloan, R. E. Kalina, A. E. Hendrickson, *J. Comp. Neurol.* **1990**, *292*, 497.

[30] T. L. Wong, Z. Yun, G. Ambur, J. Etter, in *Digit. Opt. Technol. 2017*, **2017**, 103350E.

[31] A. Maimone, J. Wang, *ACM Trans. Graph.* **2020**, *39*, 67.

[32] J. Ratcliff, A. Supikov, S. Alfaro, R. Azuma, *IEEE Trans. Vis. Comput. Graph.* **2020**, *26*, 1981.

[33] H. S. Park, R. Hoskinson, H. Abdollahi, B. Stoeber, *Opt. Express* **2015**, *23*, 30618.

[34] K. Bang, Y. Jo, M. Chae, B. Lee, *IEEE Trans. Vis. Comput. Graph.* **2021**, *27*, 2545.

[35] A. Frommer, in *SPIE AVR21 Industry Talks II*, SPIE, Bellingham, WA **2021**, p. 3.

[36] H. Boo, Y. S. Lee, H. Yang, B. Matthews, T. G. Lee, C. W. Wong, *Sci. Rep.* **2022**, *12*, 5832.

[37] A. Ghosh, E. P. Donoghue, I. Khayrullin, T. Ali, I. Wacyk, K. Tice, F. Vazan, L. Sziklas, D. Fellowes, R. Draper, *Dig. Tech. Pap. - Soc. Inf. Disp. Int. Symp.* **2016**, *47*, 837.

[38] A. Ghosh, E. P. Donoghue, I. Khayrullin, T. Ali, I. Wackyk, K. Tice, F. Vazan, O. Prache, Q. Wang, L. Sziklas, D. Fellowes, R. Draper, *Dig. Tech. Pap. - Soc. Inf. Disp. Int. Symp.* **2017**, *48*, 226.

[39] P. LU, G. Huang, S. Yang, X. Chen, X. Dong, H. Wang, Y. Wang, M. Xuan, C. Zhang, M. Yang, C. Wang, H. Yue, *SID Symp. Dig. Tech. Pap.* **2019**, *50*, 725.

[40] S. K. Kim, M. J. Park, R. Lampande, S. W. Jung, H. Park, J. K. Jeong, J. H. Kwon, *Org. Electron.* **2020**, *87*, 105938.

[41] R. Pfeifer, K. Fehse, U. Vogel, K. Leo, in *2011 Semiconductor Conference Dresden*, IEEE, Piscataway, NJ **2011**, pp. 1–4.

[42] Y. Motoyama, K. Sugiyama, H. Tanaka, H. Tsuchioka, K. Matsusaki, H. Fukumoto, *J. Soc. Inf. Disp.* **2019**, *27*, 354.

[43] W.-J. Joo, J. Kyoung, M. Esfandyarpour, S.-H. Lee, H. Koo, S. Song, Y.-N. Kwon, S. H. Song, J. C. Bae, A. Jo, M.-J. Kwon, S. H. Han, S.-H. Kim, S. Hwang, M. L. Brongersma, *Science* **2020**, *370*, 459.

[44] Z. Zhuang, D. Iida, K. Ohkawa, *Jpn. J. Appl. Phys.* **2022**, *61*, SA0809.

[45] S. S. Pasayat, C. Gupta, M. S. Wong, R. Ley, M. J. Gordon, S. P. DenBaars, S. Nakamura, S. Keller, U. K. Mishra, *Appl. Phys. Express* **2021**, *14*, 011004.

[46] X. Liu, Y. Wu, Y. Malhotra, Y. Sun, Y. Ra, R. Wang, M. Stevenson, S. Coe-Sullivan, Z. Mi, *J. Soc. Inf. Disp.* **2020**, *28*, 410.

[47] K. Fan, J. Tao, Y. Zhao, P. Li, W. Sun, L. Zhu, J. Lv, Y. Qin, Q. Wang, J. Liang, W. Wang, *Results Phys.* **2022**, *36*, 105449.

[48] A. R. Anwar, M. T. Sajjad, M. A. Johar, C. A. Hernández-Gutiérrez, M. Usman, S. P. Łepkowski, *Laser Photonics Rev.* **2022**, *16*, 2100427.

[49] E. Hsiang, Z. Yang, Q. Yang, Y. Lan, S. Wu, *J. Soc. Inf. Disp.* **2021**, *29*, 446.

[50] Y. Cai, C. Zhu, W. Zhong, P. Feng, S. Jiang, T. Wang, *Adv. Mater. Technol.* **2021**, *6*, 2100214.

[51] S. Hwangbo, L. Hu, A. T. Hoang, J. Y. Choi, J.-H. Ahn, *Nat. Nanotechnol.* **2022**, *17*, 500.

[52] P. J. Parbrook, B. Corbett, J. Han, T. Seong, H. Amano, *Laser Photonics Rev.* **2021**, *15*, 2000133.

[53] J. Day, J. Li, D. Y. C. Lie, C. Bradford, J. Y. Lin, H. X. Jiang, *Appl. Phys. Lett.* **2011**, *99*, 031116.

[54] J. G. Um, D. Y. Jeong, Y. Jung, J. K. Moon, Y. H. Jung, S. Kim, S. H. Kim, J. S. Lee, J. Jang, *Adv. Electron. Mater.* **2019**, *5*, 1800617.

[55] Y. Zhao, J. Liang, Q. Zeng, Y. Li, P. Li, K. Fan, W. Sun, J. Lv, Y. Qin, Q. Wang, J. Tao, W. Wang, *Opt. Express* **2021**, *29*, 20217.

[56] L. Zhang, F. Ou, W. C. Chong, Y. Chen, Q. Li, *J. Soc. Inf. Disp.* **2018**, *26*, 137.

[57] J. McKittrick, L. E. Shea-Rohwer, *J. Am. Ceram. Soc.* **2014**, *97*, 1327.

[58] J. Owen, L. Brus, *J. Am. Chem. Soc.* **2017**, *139*, 10939.

[59] Y. Shirasaki, *Nat. Photonics* **2013**, *7*, 13.

[60] M. V. Kovalenko, L. Manna, A. Cabot, Z. Hens, D. V. Talapin, C. R. Kagan, V. I. Klimov, A. L. Rogach, P. Reiss, D. J. Milliron, P. Guyot-Sionnnest, G. Konstantatos, W. J. Parak, T. Hyeon, B. A. Korgel, C. B. Murray, W. Heiss, *ACS Nano* **2015**, *9*, 1012.

[61] J. Zhou, C. Pu, T. Jiao, X. Hou, X. Peng, *J. Am. Chem. Soc.* **2016**, *138*, 6475.

[62] Q. Sun, Y. A. Wang, L. S. Li, D. Wang, T. Zhu, J. Xu, C. Yang, Y. Li, *Nat. Photonics* **2007**, *1*, 717.

[63] B. Chen, D. Li, F. Wang, *Small* **2020**, *16*, 2002454.

[64] A. L. Efros, D. J. Nesbitt, *Nat. Nanotechnol.* **2016**, *11*, 661.

[65] D. Vasudevan, R. R. Gaddam, A. Trinchi, I. Cole, *J. Alloys Compd.* **2015**, *636*, 395.

[66] M. Yin, Z. Yu, T. Pan, X. Peng, X. Zhang, L. Zhang, W. Xie, *Org. Electron.* **2018**, *56*, 46.

[67] Y. Wang, V. D. Ta, Y. Gao, T. C. He, R. Chen, E. Mutlugun, H. V. Demir, H. D. Sun, *Adv. Mater.* **2014**, *26*, 2954.

[68] B. C. Fitzmorris, J. K. Cooper, J. Edberg, S. Gul, J. Guo, J. Z. Zhang, *J. Phys. Chem. C* **2012**, *116*, 25065.

[69] P. N. Goswami, D. Mandal, A. K. Rath, *Nanoscale* **2018**, *10*, 1072.

[70] I. V. Martynenko, A. S. Baimuratov, V. A. Osipova, V. A. Kuznetsova, F. Purcell-Milton, I. D. Rukhlenko, A. V. Fedorov, Y. K. Gun'ko, U. Resch-Genger, A. V. Baranov, *Chem. Mater.* **2018**, *30*, 465.

[71] Z. Wu, P. Liu, W. Zhang, K. Wang, X. W. Sun, *ACS Energy Lett.* **2020**, *5*, 1095.

[72] Y. Suh, S. Lee, S. Jung, S. Y. Bang, J. Yang, X. Fan, S. Zhan, C. Samarakoon, J. Jo, Y. Kim, H. W. Choi, L. G. Occhipinti, T. H. Lee, D. Shin, J. M. Kim, *Adv. Opt. Mater.* **2022**, *10*, 2102372.

[73] Y.-H. Won, O. Cho, T. Kim, D.-Y. Chung, T. Kim, H. Chung, H. Jang, J. Lee, D. Kim, E. Jang, *Nature* **2019**, *575*, 634.

[74] X. Shan, B. Li, B. Ji, *Chem. Mater.* **2021**, *33*, 5223.

[75] V. Srivastava, V. Kamysbayev, L. Hong, E. Dunietz, R. F. Klie, D. V. Talapin, *J. Am. Chem. Soc.* **2018**, *140*, 12144.

[76] D. A. Taylor, J. A. Teku, S. Cho, W.-S. Chae, S.-J. Jeong, J.-S. Lee, *Chem. Mater.* **2021**, *33*, 4399.

[77] W.-C. Chao, T.-H. Chiang, Y.-C. Liu, Z.-X. Huang, C.-C. Liao, C.-H. Chu, C.-H. Wang, H.-W. Tseng, W.-Y. Hung, P.-T. Chou, *Commun. Mater.* **2021**, *2*, 96.

[78] D. C. Gary, B. A. Glassy, B. M. Cossairt, *Chem. Mater.* **2014**, *26*, 1734.

[79] J.-H. Jo, D.-Y. Jo, S.-H. Lee, S.-Y. Yoon, H.-B. Lim, B.-J. Lee, Y. R. Do, H. Yang, *ACS Appl. Nano Mater.* **2020**, *3*, 1972.

[80] Y. Kim, S. Ham, H. Jang, J. H. Min, H. Chung, J. Lee, D. Kim, E. Jang, *ACS Appl. Nano Mater.* **2019**, *2*, 1496.

[81] W. Yin, M. Li, W. Dong, Z. Luo, Y. Li, J. Qian, J. Zhang, W. Zhang, Y. Zhang, S. V. Kershaw, X. Zhang, W. Zheng, A. L. Rogach, *ACS Energy Lett.* **2021**, *6*, 477.

[82] P. Ramasamy, K.-J. Ko, J.-W. Kang, J.-S. Lee, *Chem. Mater.* **2018**, *30*, 3643.

[83] J. J. Calvin, J. K. Swabeck, A. B. Sedlak, Y. Kim, E. Jang, A. P. Alivisatos, *J. Am. Chem. Soc.* **2020**, *142*, 18897.

[84] T.-G. Kim, D. Zherebetskyy, Y. Bekenstein, M. H. Oh, L.-W. Wang, E. Jang, A. P. Alivisatos, *ACS Nano* **2018**, *12*, 11529.

[85] K.-H. Kim, J.-H. Jo, D.-Y. Jo, C.-Y. Han, S.-Y. Yoon, Y. Kim, Y.-H. Kim, Y. H. Ko, S. W. Kim, C. Lee, H. Yang, *Chem. Mater.* **2020**, *32*, 3537.

[86] Z. Liu, C.-H. Lin, B.-R. Hyun, C.-W. Sher, Z. Lv, B. Luo, F. Jiang, T. Wu, C.-H. Ho, H.-C. Kuo, J.-H. He, *Light: Sci Appl* **2020**, *9*, 83.

[87] R. Zhu, Z. Luo, H. Chen, Y. Dong, S.-T. Wu, *Opt. Express* **2015**, *23*, 23680.
[88] Y. Wei, Z. Cheng, J. Lin, *Chem. Soc. Rev.* **2019**, *48*, 310.
[89] W. Travis, E. N. K. Glover, H. Bronstein, D. O. Scanlon, R. G. Palgrave, *Chem. Sci.* **2016**, *7*, 4548.
[90] X. Li, X. Gao, X. Zhang, X. Shen, M. Lu, J. Wu, Z. Shi, V. L. Colvin, J. Hu, X. Bai, W. W. Yu, Y. Zhang, *Adv. Sci.* **2021**, *8*, 2003334.
[91] J. Kim, S.-H. Lee, J. H. Lee, K.-H. Hong, *J. Phys. Chem. Lett.* **2014**, *5*, 1312.
[92] M. Kim, H. Jun, H. Lee, H. Nahdi, D. Tondelier, Y. Bonnassieux, J. Bourée, B. Geffroy, *Eur. J. Inorg. Chem.* **2021**, *2021*, 4781.
[93] W.-J. Yin, T. Shi, Y. Yan, *Adv. Mater.* **2014**, *26*, 4653.
[94] R. E. Brandt, J. R. Poindexter, P. Gorai, R. C. Kurchin, R. L. Z. Hoye, L. Nienhaus, M. W. B. Wilson, J. A. Polizzotti, R. Sereika, R. Žaltauskas, L. C. Lee, J. L. MacManus-Driscoll, M. Bawendi, V. Stevanović, T. Buonassisi, *Chem. Mater.* **2017**, *29*, 4667.
[95] H. Huang, M. I. Bodnarchuk, S. V. Kershaw, M. V. Kovalenko, A. L. Rogach, *ACS Energy Lett.* **2017**, *2*, 2071.
[96] J. Shamsi, G. Rainò, M. V. Kovalenko, S. D. Stranks, *Nat. Nanotechnol.* **2021**, *16*, 1164.
[97] L. Protesescu, S. Yakunin, M. I. Bodnarchuk, F. Krieg, R. Caputo, C. H. Hendon, R. X. Yang, A. Walsh, M. V. Kovalenko, *Nano Lett.* **2015**, *15*, 3692.
[98] I. Lignos, R. M. Maceiczyk, M. V. Kovalenko, S. Stavrakis, *Chem. Mater.* **2020**, *32*, 27.
[99] H. Cho, S.-H. Jeong, M.-H. Park, Y.-H. Kim, C. Wolf, C.-L. Lee, J. H. Heo, A. Sadhanala, N. Myoung, S. Yoo, S. H. Im, R. H. Friend, T.-W. Lee, *Science* **2015**, *350*, 1222.
[100] Y.-H. Kim, C. Wolf, Y.-T. Kim, H. Cho, W. Kwon, S. Do, A. Sadhanala, C. G. Park, S.-W. Rhee, S. H. Im, R. H. Friend, T.-W. Lee, *ACS Nano* **2017**, *11*, 6586.
[101] C. Lee, Y. Shin, A. Villanueva-Antolí, S. Das Adhikari, J. Rodriguez-Pereira, J. M. Macak, C. A. Mesa, S. Giménez, S. J. Yoon, A. F. Gualdrón-Reyes, I. Mora-Seró, *Chem. Mater.* **2021**, *33*, 8745.
[102] Z. Chu, Q. Ye, Y. Zhao, F. Ma, Z. Yin, X. Zhang, J. You, *Adv. Mater.* **2021**, *33*, 2007169.
[103] A. F. Gualdrón-Reyes, S. Masi, I. Mora-Seró, *Trends Chem.* **2021**, *3*, 499.
[104] H. Lee, H. Kim, H. Cho, W. Cha, Y. Hong, Y. Kim, A. Sadhanala, V. Venugopalan, J. S. Kim, J. W. Choi, C. Lee, D. Kim, H. Yang, R. H. Friend, T. Lee, *Adv. Funct. Mater.* **2019**, *29*, 1901225.
[105] J. Yin, H. Yang, L. Gutiérrez-Arzaluz, Y. Zhou, J.-L. Brédas, O. M. Bakr, O. F. Mohammed, *ACS Nano* **2021**, *15*, 17998.
[106] I. Lignos, S. Stavrakis, G. Nedelcu, L. Protesescu, A. J. DeMello, M. V. Kovalenko, *Nano Lett.* **2016**, *16*, 1869.
[107] Q. A. Akkerman, S. Park, E. Radicchi, F. Nunzi, E. Mosconi, F. De Angelis, R. Brescia, P. Rastogi, M. Prato, L. Manna, *Nano Lett.* **2017**, *17*, 1924.
[108] S. Bera, R. K. Behera, N. Pradhan, *J. Am. Chem. Soc.* **2020**, *142*, 20865.
[109] Y.-H. Kim, G.-H. Lee, Y.-T. Kim, C. Wolf, H. J. Yun, W. Kwon, C. G. Park, T.-W. Lee, *Nano Energy* **2017**, *38*, 51.
[110] Y. Zhang, T. D. Siegler, C. J. Thomas, M. K. Abney, T. Shah, A. De Gorostiza, R. M. Greene, B. A. Korgel, *Chem. Mater.* **2020**, *32*, 5410.
[111] J. Zhang, C. Yin, F. Yang, Y. Yao, F. Yuan, H. Chen, R. Wang, S. Bai, G. Tu, L. Hou, *J. Phys. Chem. Lett.* **2021**, *12*, 2437.
[112] S. Paul, A. Samanta, *ACS Energy Lett.* **2020**, *5*, 64.
[113] S. Seth, T. Ahmed, A. De, A. Samanta, *ACS Energy Lett.* **2019**, *4*, 1610.
[114] J. Xue, R. Wang, Y. Yang, *Nat. Rev. Mater.* **2020**, *5*, 809.
[115] M. Imran, V. Caligiuri, M. Wang, L. Goldoni, M. Prato, R. Krahne, L. De Trizio, L. Manna, *J. Am. Chem. Soc.* **2018**, *140*, 2656.
[116] D. Yoo, J. Y. Woo, Y. Kim, S. W. Kim, S.-H. Wei, S. Jeong, Y.-H. Kim, *J. Phys. Chem. Lett.* **2020**, *11*, 652.
[117] K. Hills-Kimball, H. Yang, T. Cai, J. Wang, O. Chen, *Adv. Sci.* **2021**, *8*, 2100214.
[118] F. McGrath, U. V. Ghorpade, K. M. Ryan, *J. Chem. Phys.* **2020**, *152*, 174702.
[119] D. Yang, X. Li, W. Zhou, S. Zhang, C. Meng, Y. Wu, Y. Wang, H. Zeng, *Adv. Mater.* **2019**, *31*, 1900767.
[120] F. Krieg, S. T. Ochsenbein, S. Yakunin, S. ten Brinck, P. Aellen, A. Süess, B. Clerc, D. Guggisberg, O. Nazarenko, Y. Shynkarenko, S. Kumar, C.-J. Shih, I. Infante, M. V. Kovalenko, *ACS Energy Lett.* **2018**, *3*, 641.
[121] B. Zhang, L. Goldoni, J. Zito, Z. Dang, G. Almeida, F. Zaccaria, J. de Wit, I. Infante, L. De Trizio, L. Manna, *Chem. Mater.* **2019**, *31*, 9140.
[122] G. H. Ahmed, J. Yin, O. M. Bakr, O. F. Mohammed, *ACS Energy Lett.* **2021**, *6*, 1340.
[123] C. Zhang, S. Wang, X. Li, M. Yuan, L. Turyanska, X. Yang, *Adv. Funct. Mater.* **2020**, *30*, 1910582.
[124] A. Dey, J. Ye, A. De, E. Debroye, S. K. Ha, E. Bladt, A. S. Kshirsagar, Z. Wang, J. Yin, Y. Wang, L. N. Quan, F. Yan, M. Gao, X. Li, J. Shamsi, T. Debnath, M. Cao, M. A. Scheel, S. Kumar, J. A. Steele, M. Gerhard, L. Chouhan, K. Xu, X. Wu, Y. Li, Y. Zhang, A. Dutta, C. Han, I. Vincon, A. L. Rogach, et al, *ACS Nano* **2021**, *15*, 10775.
[125] M. Lu, X. Zhang, X. Bai, H. Wu, X. Shen, Y. Zhang, W. Zhang, W. Zheng, H. Song, W. W. Yu, A. L. Rogach, *ACS Energy Lett.* **2018**, *3*, 1571.
[126] Y. Xie, B. Peng, I. Bravić, Y. Yu, Y. Dong, R. Liang, Q. Ou, B. Monserrat, S. Zhang, *Adv. Sci.* **2020**, *7*, 2001698.
[127] H. Kim, S. Bae, T. H. Lee, H. Lee, H. Kang, S. Park, H. W. Jang, S. Y. Kim, *Adv. Funct. Mater.* **2021**, *31*, 2102770.
[128] Z. Shi, J. Guo, Y. Chen, Q. Li, Y. Pan, H. Zhang, Y. Xia, W. Huang, *Adv. Mater.* **2017**, *29*, 1605005.
[129] P. Su, Y. Liu, J. Zhang, C. Chen, B. Yang, C. Zhang, X. Zhao, *J. Phys. Chem. Lett.* **2020**, *11*, 2812.
[130] J. Sun, J. Yang, J. I. Lee, J. H. Cho, M. S. Kang, *J. Phys. Chem. Lett.* **2018**, *9*, 1573.
[131] H. Liang, F. Yuan, A. Johnston, C. Gao, H. Choubisa, Y. Gao, Y. Wang, L. K. Sagar, B. Sun, P. Li, G. Bappi, B. Chen, J. Li, Y. Wang, Y. Dong, D. Ma, Y. Gao, Y. Liu, M. Yuan, M. I. Saidaminov, S. Hoogland, Z. Lu, E. H. Sargent, *Adv. Sci.* **2020**, *7*, 1903213.
[132] C. Gao, Y. Jiang, C. Sun, J. Han, T. He, Y. Huang, K. Yao, M. Han, X. Wang, Y. Wang, Y. Gao, Y. Liu, M. Yuan, H. Liang, *ACS Photonics* **2020**, *7*, 1915.
[133] A. G. Kontos, A. Kaltzoglou, E. Siranidi, D. Palles, G. K. Angeli, M. K. Arfanis, V. Psycharis, Y. S. Raptis, E. I. Kamitsos, P. N. Trikalitis, C. C. Stoumpos, M. G. Kanatzidis, P. Falaras, *Inorg. Chem.* **2017**, *56*, 84.
[134] Q. Liu, J. Yin, B.-B. Zhang, J.-K. Chen, Y. Zhou, L.-M. Zhang, L.-M. Wang, Q. Zhao, J. Hou, J. Shu, B. Song, N. Shirahata, O. M. Bakr, O. F. Mohammed, H.-T. Sun, *J. Am. Chem. Soc.* **2021**, *143*, 5470.
[135] J. Luo, L. Yang, Z. Tan, W. Xie, Q. Sun, J. Li, P. Du, Q. Xiao, L. Wang, X. Zhao, G. Niu, L. Gao, S. Jin, J. Tang, *Adv. Mater.* **2021**, *33*, 2101903.
[136] S. Kachhap, S. Singh, A. K. Singh, S. K. Singh, *J. Mater. Chem. C* **2022**, *10*, 3647.
[137] J. Huang, T. Lei, M. Siron, Y. Zhang, S. Yu, F. Seeler, A. Dehestani, L. N. Quan, K. Schierle-Arndt, P. Yang, *Nano Lett.* **2020**, *20*, 3734.
[138] J. Pal, S. Manna, A. Mondal, S. Das, K. V. Adarsh, A. Nag, *Angew. Chem.* **2017**, *129*, 14375.
[139] Z. Ma, Z. Shi, D. Yang, F. Zhang, S. Li, L. Wang, D. Wu, Y. Zhang, G. Na, L. Zhang, X. Li, Y. Zhang, C. Shan, *ACS Energy Lett.* **2020**, *5*, 385.
[140] J. Zhang, L. Zhang, P. Cai, X. Xue, M. Wang, J. Zhang, G. Tu, *Nano Energy* **2019**, *62*, 434.

[141] P. Yang, G. Liu, B. Liu, X. Liu, Y. Lou, J. Chen, Y. Zhao, *Chem. Commun.* **2018**, *54*, 11638.
[142] L. Wang, Z. Shi, Z. Ma, D. Yang, F. Zhang, X. Ji, M. Wang, X. Chen, G. Na, S. Chen, D. Wu, Y. Zhang, X. Li, L. Zhang, C. Shan, *Nano Lett.* **2020**, *20*, 3568.
[143] Q. Fan, G. V. Biesold-McGee, J. Ma, Q. Xu, S. Pan, J. Peng, Z. Lin, *Angew. Chem., Int. Ed.* **2020**, *59*, 1030.
[144] B. Yang, K. Han, *J. Phys. Chem. Lett.* **2021**, *12*, 8256.
[145] M. Yao, L. Wang, J. Yao, K. Wang, C. Chen, B. Zhu, J. Yang, J. Wang, W. Xu, Q. Zhang, H. Yao, *Adv. Opt. Mater.* **2020**, *8*, 1901919.
[146] B. Ke, R. Zeng, Z. Zhao, Q. Wei, X. Xue, K. Bai, C. Cai, W. Zhou, Z. Xia, B. Zou, *J. Phys. Chem. Lett.* **2020**, *11*, 340.
[147] F. Locardi, E. Sartori, J. Buha, J. Zito, M. Prato, V. Pinchetti, M. L. Zaffalon, M. Ferretti, S. Brovelli, I. Infante, L. De Trizio, L. Manna, *ACS Energy Lett.* **2019**, *4*, 1976.
[148] X. Su, L. Lian, C. Zhang, J. Zhang, S. Liu, S. Zhu, Y. Gao, W. Luo, H. Li, D. Zhang, *Adv. Opt. Mater.* **2021**, *9*, 2001866.
[149] S. Jin, R. Li, H. Huang, N. Jiang, J. Lin, S. Wang, Y. Zheng, X. Chen, D. Chen, *Light: Sci Appl* **2022**, *11*, 52.
[150] J. Zhao, L. Chen, D. Li, Z. Shi, P. Liu, Z. Yao, H. Yang, T. Zou, B. Zhao, X. Zhang, H. Zhou, Y. Yang, W. Cao, X. Yan, S. Zhang, X. W. Sun, *Nat. Commun.* **2021**, *12*, 4603.
[151] T. Zhan, K. Yin, J. Xiong, Z. He, S. Wu, *iScience* **2020**, *23*, 101397.
[152] X. Zhou, Y. Cai, M. Xu, J. Li, C. Sheng, Q. Zhang, X. Qiu, W. Wang, S. Xiong, C. Cong, Z. Qiu, R. Liu, L. Hu, *Small Methods* **2022**, *6*, 2101509.
[153] K. Parikh, J. Zhuang, K. Pallister, J. Jiang, M. Smith, *Dig. Tech. Pap. - Soc. Inf. Disp. Int. Symp.* **2018**, *49*, 502.
[154] R. Wang, Y. Liang, M. Zhao, Z. Chen, L. Zhou, L. Wang, G. Yu, L. Liu, Z. Xie, J. Peng, Y. Cao, *Adv. Opt. Mater.* **2022**, *10*, 2101521.
[155] C. Anthes, M. Wiedemann, D. Kranzlmüller, in *2016 IEEE Aerospace Conf.*, IEEE, Big Sky, MT **2016**, pp. 1–19.
[156] K. Masaoka, Y. Nishida, M. Sugawara, *Opt. Express* **2014**, *22*, 19069.
[157] H. Cho, J. Pan, H. Wu, X. Lan, I. Coropceanu, Y. Wang, W. Cho, E. A. Hill, J. S. Anderson, D. V. Talapin, *Adv. Mater.* **2020**, *32*, 2003805.
[158] Y. Wang, I. Fedin, H. Zhang, D. V. Talapin, *Science* **2017**, *357*, 385.
[159] J. Sun, B. Bao, M. He, H. Zhou, Y. Song, *ACS Appl. Mater. Interfaces* **2015**, *7*, 28086.
[160] D. Hahm, J. Lim, H. Kim, J.-W. Shin, S. Hwang, S. Rhee, J. H. Chang, J. Yang, C. H. Lim, H. Jo, B. Choi, N. S. Cho, Y.-S. Park, D. C. Lee, E. Hwang, S. Chung, C. Kang, M. S. Kang, W. K. Bae, *Nat. Nanotechnol.* **2022**, *17*, 952.
[161] T. Ji, S. Jin, H. Zhang, S. Chen, X. W. Sun, *J. Soc. Inf. Disp.* **2018**, *26*, 121.
[162] C. Zou, C. Chang, D. Sun, K. F. Böhringer, L. Y. Lin, *Nano Lett.* **2020**, *20*, 3710.
[163] J. Harwell, J. Burch, A. Fikouras, M. C. Gather, A. Di Falco, I. D. W. Samuel, *ACS Nano* **2019**, *13*, 3823.
[164] G.-H. Kim, J. Lee, J. Y. Lee, J. Han, Y. Choi, C. J. Kang, K.-B. Kim, W. Lee, J. Lim, S.-Y. Cho, *ACS Appl. Mater. Interfaces* **2021**, *13*, 43075.
[165] T. Imae, *Curr. Opin. Colloid Interface Sci.* **2003**, *8*, 307.
[166] C. H. Lin, Q. Zeng, E. Lafalce, S. Yu, M. J. Smith, Y. J. Yoon, Y. Chang, Y. Jiang, Z. Lin, Z. V. Vardeny, V. V. Tsukruk, *Adv. Opt. Mater.* **2018**, *6*, 1800474.
[167] G. Zhang, H. Zhang, R. Yu, Y. Duan, Y. Huang, Z. Yin, *ACS Appl. Mater. Interfaces* **2022**, *14*, 14712.
[168] X. Yuan, Z. Xiong, *J. Micromech. Microeng.* **2018**, *28*, 095008.
[169] H. Li, Y. Duan, Z. Shao, G. Zhang, H. Li, Y. Huang, Z. Yin, *Adv. Mater. Technol.* **2020**, *5*, 2000401.
[170] P. Yang, L. Zhang, D. J. Kang, R. Strahl, T. Kraus, *Adv. Opt. Mater.* **2020**, *8*, 1901429.
[171] C. Jiang, Z. Zhong, B. Liu, Z. He, J. Zou, L. Wang, J. Wang, J. Peng, Y. Cao, *ACS Appl. Mater. Interfaces* **2016**, *8*, 26162.
[172] C. Wei, W. Su, J. Li, B. Xu, Q. Shan, Y. Wu, F. Zhang, M. Luo, H. Xiang, Z. Cui, H. Zeng, *Adv. Mater.* **2022**, *34*, 2107798.
[173] Y. Liu, F. Li, L. Qiu, K. Yang, Q. Li, X. Zheng, H. Hu, T. Guo, C. Wu, T. W. Kim, *ACS Nano* **2019**, *13*, 2041.
[174] L. Kim, P. O. Anikeeva, S. A. Coe-Sullivan, J. S. Steckel, M. G. Bawendi, V. Bulović, *Nano Lett.* **2008**, *8*, 4513.
[175] T.-H. Kim, K.-S. Cho, E. K. Lee, S. J. Lee, J. Chae, J. W. Kim, D. H. Kim, J.-Y. Kwon, G. Amaratunga, S. Y. Lee, B. L. Choi, Y. Kuk, J. M. Kim, K. Kim, *Nat. Photonics* **2011**, *5*, 176.
[176] B. H. Kim, S. Nam, N. Oh, S.-Y. Cho, K. J. Yu, C. H. Lee, J. Zhang, K. Deshpande, P. Trefonas, J.-H. Kim, J. Lee, J. H. Shin, Y. Yu, J. Bin Lim, S. M. Won, Y. K. Cho, N. H. Kim, K. J. Seo, H. Lee, T. Kim, M. Shim, J. A. Rogers, *ACS Nano* **2016**, *10*, 4920.
[177] M. K. Choi, J. Yang, K. Kang, D. C. Kim, C. Choi, C. Park, S. J. Kim, S. I. Chae, T.-H. Kim, J. H. Kim, T. Hyeon, D.-H. Kim, *Nat. Commun.* **2015**, *6*, 7149.
[178] T. W. Nam, M. Kim, Y. Wang, G. Y. Kim, W. Choi, H. Lim, K. M. Song, M.-J. Choi, D. Y. Jeon, J. C. Grossman, Y. S. Jung, *Nat. Commun.* **2020**, *11*, 3040.
[179] W. Zhan, L. Meng, C. Shao, X. Wu, K. Shi, H. Zhong, *ACS Photonics* **2021**, *8*, 765.
[180] X. Huang, Q. Guo, S. Kang, T. Ouyang, Q. Chen, X. Liu, Z. Xia, Z. Yang, Q. Zhang, J. Qiu, G. Dong, *ACS Nano* **2020**, *14*, 3150.
[181] Y. Wang, J.-A. Pan, H. Wu, D. V. Talapin, *ACS Nano* **2019**, *13*, 13917.
[182] M. V Kovalenko, M. I. Bodnarchuk, J. Zaumseil, J. Lee, D. V Talapin, *J. Am. Chem. Soc.* **2010**, *132*, 10085.
[183] J.-A. Pan, J. C. Ondry, D. V. Talapin, *Nano Lett.* **2021**, *21*, 7609.
[184] F. Palazon, Q. A. Akkerman, M. Prato, L. Manna, *ACS Nano* **2016**, *10*, 1224.
[185] L. Wang, Y. Zhu, H. Liu, J. Gong, W. Wang, S. Guo, Y. Yu, H. Peng, Y. Liao, *ACS Appl. Mater. Interfaces* **2019**, *11*, 35270.
[186] C. D. Dieleman, W. Ding, L. Wu, N. Thakur, I. Bespalov, B. Daiber, Y. Ekinci, S. Castellanos, B. Ehrler, *Nanoscale* **2020**, *12*, 11306.
[187] S. Jun, E. Jang, J. Park, J. Kim, *Langmuir* **2006**, *22*, 2407.
[188] J. Ko, K. Ma, J. F. Joung, S. Park, J. Bang, *Nano Lett.* **2021**, *21*, 2288.
[189] B. M. Oh, Y. Jeong, J. Zheng, N. Y. Cho, M. Song, J. W. Choi, J. H. Kim, *Chem. Commun.* **2021**, *57*, 12824.
[190] D. Liu, K. Weng, S. Lu, F. Li, H. Abudukeremu, L. Zhang, Y. Yang, J. Hou, H. Qiu, Z. Fu, X. Luo, L. Duan, Y. Zhang, H. Zhang, J. Li, *Sci. Adv.* **2022**, *8*, eabm8433.
[191] J. Yang, D. Hahm, K. Kim, S. Rhee, M. Lee, S. Kim, J. H. Chang, H. W. Park, J. Lim, M. Lee, H. Kim, J. Bang, H. Ahn, J. H. Cho, J. Kwak, B. Kim, C. Lee, W. K. Bae, M. S. Kang, *Nat. Commun.* **2020**, *11*, 2874.
[192] S. Lu, Z. Fu, F. Li, K. Weng, L. Zhou, L. Zhang, Y. Yang, H. Qiu, D. Liu, W. Qing, H. Ding, X. Sheng, M. Chen, X. Tang, L. Duan, W. Liu, L. Wu, Y. Yang, H. Zhang, J. Li, *Angew. Chem., Int. Ed.* **2022**, *61*, e202202633.
[193] J. Park, H. M. Jang, S. Kim, S. H. Jo, T.-W. Lee, *Trends Chem.* **2020**, *2*, 837.
[194] J. S. Steckel, J. Ho, C. Hamilton, J. Xi, C. Breen, W. Liu, P. Allen, S. Coe-Sullivan, *J. Soc. Inf. Disp.* **2015**, *23*, 294.
[195] J. Zou, T. Zhan, E.-L. Hsiang, X. Du, X. Yu, K. Li, S.-T. Wu, *Opt. Express* **2021**, *29*, 20673.
[196] Y. Wang, F. Yuan, Y. Dong, J. Li, A. Johnston, B. Chen, M. I. Saidaminov, C. Zhou, X. Zheng, Y. Hou, K. Bertens, H. Ebe, D. Ma, Z. Deng, S. Yuan, R. Chen, L. K. Sagar, J. Liu, J. Fan, P. Li, X. Li, Y. Gao, M. Fung, Z. Lu, O. M. Bakr, L. Liao, E. H. Sargent, *Angew. Chem., Int. Ed.* **2021**, *60*, 16164.
[197] S. Coe-Sullivan, W. Liu, P. Allen, J. S. Steckel, *ECS J. Solid State Sci. Technol.* **2013**, *2*, R3026.

[198] Y.-H. Ko, P. Prabhakaran, S. Choi, G.-J. Kim, C. Lee, K.-S. Lee, *Sci. Rep.* **2020**, *10*, 15817.

[199] C. Hotz, J. Yurek, in *Advanced Display Technology*, Springer, Singapore **2021**, pp. 229–250.

[200] R. Tangirala, E. Lee, C. Sunderland, W. Guo, A. Mamuye, K. Wang, E. Hwang, N. Kim, C. Hotz, *Dig. Tech. Pap. - Soc. Inf. Disp. Int. Symp.* **2021**, *52*, 906.

[201] Y. Shirasaki, G. J. Supran, M. G. Bawendi, V. Bulović, *Nat. Photonics* **2013**, *7*, 13.

[202] A. K. Srivastava, W. Zhang, J. Schneider, J. E. Halpert, A. L. Rogach, *Adv. Sci.* **2019**, *6*, 1901345.

[203] E. Lee, R. Tangirala, A. Smith, A. Carpenter, C. Hotz, H. Kim, J. Yurek, T. Miki, S. Yoshihara, T. Kizaki, A. Ishizuka, I. Kiyoto, *Dig. Tech. Pap. - Soc. Inf. Disp. Int. Symp.* **2018**, *49*, 525.

[204] X. Li, D. Kundaliya, Z. J. Tan, M. Anc, N. X. Fang, *Opt. Express* **2019**, *27*, 30864.

[205] H.-Y. Lin, C.-W. Sher, D.-H. Hsieh, X.-Y. Chen, H.-M. P. Chen, T.-M. Chen, K.-M. Lau, C.-H. Chen, C.-C. Lin, H.-C. Kuo, *Photonics Res.* **2017**, *5*, 411.

[206] D. N. Dirin, L. Protesescu, D. Trummer, I. V. Kochetygov, S. Yakunin, F. Krumeich, N. P. Stadie, M. V. Kovalenko, *Nano Lett.* **2016**, *16*, 5866.

[207] D. H. Park, J. S. Han, W. Kim, H. S. Jang, *Dyes Pigm.* **2018**, *149*, 246.

[208] Y. Xin, H. Zhao, J. Zhang, *ACS Appl. Mater. Interfaces* **2018**, *10*, 4971.

[209] M. Meyns, M. Perálvarez, A. Heuer-Jungemann, W. Hertog, M. Ibáñez, R. Nafria, A. Genç, J. Arbiol, M. V. Kovalenko, J. Carreras, A. Cabot, A. G. Kanaras, *ACS Appl. Mater. Interfaces* **2016**, *8*, 19579.

[210] Y. Wei, X. Deng, Z. Xie, X. Cai, S. Liang, P. Ma, Z. Hou, Z. Cheng, J. Lin, *Adv. Funct. Mater.* **2017**, *27*, 1703535.

[211] S. Pathak, N. Sakai, F. Wisnivesky Rocca Rivarola, S. D. Stranks, J. Liu, G. E. Eperon, C. Ducati, K. Wojciechowski, J. T. Griffiths, A. A. Haghighirad, A. Pellaroque, R. H. Friend, H. J. Snaith, *Chem. Mater.* **2015**, *27*, 8066.

[212] Y. Wang, J. He, H. Chen, J. Chen, R. Zhu, P. Ma, A. Towers, Y. Lin, A. J. Gesquiere, S. Wu, Y. Dong, *Adv. Mater.* **2016**, *28*, 10710.

[213] H. Liao, S. Guo, S. Cao, L. Wang, F. Gao, Z. Yang, J. Zheng, W. Yang, *Adv. Opt. Mater.* **2018**, *6*, 1800346.

[214] Q. Zhou, Z. Bai, W. Lu, Y. Wang, B. Zou, H. Zhong, *Adv. Mater.* **2016**, *28*, 9163.

[215] H. Zhang, X. Wang, Q. Liao, Z. Xu, H. Li, L. Zheng, H. Fu, *Adv. Funct. Mater.* **2017**, *27*, 1604382.

[216] Y. Li, Y. Lv, Z. Guo, L. Dong, J. Zheng, C. Chai, N. Chen, Y. Lu, C. Chen, *ACS Appl. Mater. Interfaces* **2018**, *10*, 15888.

[217] W. Xu, Z. Cai, F. Li, J. Dong, Y. Wang, Y. Jiang, X. Chen, *Nano Res.* **2017**, *10*, 2692.

[218] J. Jang, Y. Kim, S. Park, D. Yoo, H. Cho, J. Jang, H. B. Jeong, H. Lee, J. M. Yuk, C. B. Park, D. Y. Jeon, Y. Kim, B. Bae, T. Lee, *Adv. Mater.* **2021**, *33*, 2005255.

[219] H. Zhou, J. Park, Y. Lee, J. Park, J. Kim, J. S. Kim, H. Lee, S. H. Jo, X. Cai, L. Li, X. Sheng, H. J. Yun, J. Park, J. Sun, T. Lee, *Adv. Mater.* **2020**, *32*, 2001989.

[220] J.-M. Park, J. Park, Y.-H. Kim, H. Zhou, Y. Lee, S. H. Jo, J. Ma, T.-W. Lee, J.-Y. Sun, *Nat. Commun.* **2020**, *11*, 4638.

[221] Y. E. Panfil, M. Oded, U. Banin, *Angew. Chem., Int. Ed.* **2018**, *57*, 4274.

[222] J. Yang, M. K. Choi, U. J. Yang, S. Y. Kim, Y. S. Kim, J. H. Kim, D.-H. Kim, T. Hyeon, *Nano Lett.* **2021**, *21*, 26.

[223] W. Zhang, Y. Tan, X. Duan, F. Zhao, H. Liu, W. Chen, P. Liu, X. Liu, K. Wang, Z. Zhang, X. W. Sun, *Adv. Opt. Mater.* **2022**, *10*, 2200685.

[224] Y. Shen, H. Wu, Y. Li, K. Shen, X. Gao, F. Song, J. Tang, *Adv. Funct. Mater.* **2021**, *31*, 2103870.

[225] S.-J. Woo, J. S. Kim, T.-W. Lee, *Nat. Photonics* **2021**, *15*, 630.

[226] Y. Deng, F. Peng, Y. Lu, X. Zhu, W. Jin, J. Qiu, J. Dong, Y. Hao, D. Di, Y. Gao, T. Sun, M. Zhang, F. Liu, L. Wang, L. Ying, F. Huang, Y. Jin, *Nat. Photonics* **2022**, *16*, 505.

[227] Y. Shen, K. Shen, Y. Li, M. Guo, J. Wang, Y. Ye, F. Xie, H. Ren, X. Gao, F. Song, J. Tang, *Adv. Funct. Mater.* **2021**, *31*, 2006736.

[228] B. Han, S. Yuan, B. Cai, J. Song, W. Liu, F. Zhang, T. Fang, C. Wei, H. Zeng, *Adv. Funct. Mater.* **2021**, *31*, 2011003.

[229] S.-H. Lee, S.-W. Song, S.-Y. Yoon, D.-Y. Jo, S.-K. Kim, H.-M. Kim, Y. Kim, S. M. Park, H. Yang, *Chem. Eng. J.* **2022**, *429*, 132464.

[230] F. Yang, H. Chen, R. Zhang, X. Liu, W. Zhang, J. Zhang, F. Gao, L. Wang, *Adv. Funct. Mater.* **2020**, *30*, 1908760.

[231] H. Jia, H. Shi, R. Yu, H. Ma, Z. Wang, C. Zou, Z. Tan, *Small* **2022**, *18*, 2200036.

[232] H. Tang, Y. Xu, X. Hu, Q. Hu, T. Chen, W. Jiang, L. Wang, W. Jiang, *Adv. Sci.* **2021**, *8*, 2004118.

[233] G. Seo, H. Jung, T. D. Creason, V. Yeddu, M. Bamidele, E. Echeverria, J. Lee, D. McIlroy, B. Saparov, D. Y. Kim, *ACS Energy Lett.* **2021**, *6*, 2584.

[234] S. Yan, W. Tian, H. Chen, K. Tang, T. Lin, G. Zhong, L. Qiu, X. Pan, W. Wang, *Adv. Funct. Mater.* **2021**, *31*, 2100855.

[235] T. Someya, M. Amagai, *Nat. Biotechnol.* **2019**, *37*, 382.

[236] B. Chu, W. Burnett, J. W. Chung, Z. Bao, *Nature* **2017**, *549*, 328.

[237] J. A. Rogers, T. Someya, Y. Huang, *Science* **2010**, *327*, 1603.

[238] T. Sekitani, H. Nakajima, H. Maeda, T. Fukushima, T. Aida, K. Hata, T. Someya, *Nat. Mater.* **2009**, *8*, 494.

[239] M. S. White, M. Kaltenbrunner, E. D. Głowacki, K. Gutnichenko, G. Kettlgruber, I. Graz, S. Aazou, C. Ulbricht, D. A. M. Egbe, M. C. Miron, Z. Major, M. C. Scharber, T. Sekitani, T. Someya, S. Bauer, N. S. Sariciftci, *Nat. Photonics* **2013**, *7*, 811.

[240] H. Zhou, J.-W. Park, *Thin Solid Films* **2016**, *619*, 281.

[241] Y. Li, S. Chou, P. Huang, C. Xiao, X. Liu, Y. Xie, F. Zhao, Y. Huang, J. Feng, H. Zhong, H. Sun, Q. Pei, *Adv. Mater.* **2019**, *31*, 1807516.

[242] S. G. R. Bade, X. Shan, P. T. Hoang, J. Li, T. Geske, L. Cai, Q. Pei, C. Wang, Z. Yu, *Adv. Mater.* **2017**, *29*, 1607053.

[243] C. Bi, Z. Yao, X. Sun, X. Wei, J. Wang, J. Tian, *Adv. Mater.* **2021**, *33*, 2006722.

[244] W. Shen, Y. Yu, W. Zhang, Y. Chen, J. Zhang, L. Yang, J. Feng, G. Cheng, L. Liu, S. Chen, *ACS Appl. Mater. Interfaces* **2022**, *14*, 5682.

[245] N. Hildebrand, "Display Daily," https://www.displaydaily.com/article/display-daily/what-does-the-convergence-of-ar-and-vr-mean-for-the-display-industry (accessed: June 2022).

[246] "Real New World," https://realnewworld.com/vr-hmd-display-technology/ (accessed: June 2022).

[247] "StradVision," https://stradvision.com/augmented-reality-head-up-display-ar-hud-provides-drivers-with-a-safer-and-more-convenient-driving-experience/ (accessed: June 2022).

[248] Y.-H. Lee, T. Zhan, S.-T. Wu, *Virtual Reality Intell. Hardware* **2019**, *1*, 10.

[249] J.-S. Park, J. Kyhm, H. H. Kim, S. Jeong, J. Kang, S. Lee, K.-T. Lee, K. Park, N. Barange, J. Han, J. D. Song, W. K. Choi, I. K. Han, *Nano Lett.* **2016**, *16*, 6946.

[250] T. Xuan, S. Shi, L. Wang, H.-C. Kuo, R.-J. Xie, *J. Phys. Chem. Lett.* **2020**, *11*, 5184.

Sun Jae Park received her M.S. degree (February 2021) from Yonsei University, Republic of Korea. Currently, she is pursuing her Ph.D. degree in Korea Advanced Institute of Science and Technology (KAIST), under the supervision of Prof. Himchan Cho. Her research interests focus on the design and synthesis of metal halide perovskites, and the patterning of nanoscale emitters.

Changmin Keum is a principal engineer in Samsung Research at Samsung Electronics. He received his Ph.D. in Electrical Engineering from Seoul National University, Republic of Korea, in 2014. He worked as a postdoctoral research associate at Kent State University, USA (2015–2016) and at the University of St. Andrews, UK (2017–2019). His research interests were in the field of organic optoelectronics, and his research currently focuses on the development of new devices and display technologies to provide AR/VR user experiences.

Himchan Cho is an assistant professor in Materials Science and Engineering at the Korea Advanced Institute of Science and Technology (KAIST). He received his Ph.D. in Materials Science and Engineering from the Pohang University of Science and Technology (POSTECH), Republic of Korea. He worked as a postdoctoral scholar at Seoul National University, Korea (2016–2018) and the University of Chicago, USA (2018–2021). His research focuses on optoelectronics applications of metal halide perovskites and colloidal quantum dots.